



RESEARCH ARTICLE

10.1002/2017JF004529

Special Section:

The Arctic: An AGU Joint Special Collection

This article is a companion to Hofstede et al. (2018), <https://doi.org/10.1002/2017JF004297>.

Key Points:

- Borehole sensors provide insight into the basal conditions and thermal structure of Store Glacier
- Fast basal motion is facilitated by inefficient subglacial drainage at high pressure and a soft bed
- Temperate basal ice is thin or absent and ice deformation is enhanced within pre-Holocene ice

Supporting Information:

- Movie S1
- Movie S2
- Movie S3
- Supporting Information S1

Correspondence to:

S. H. Doyle,
sdd08@aber.ac.uk

Citation:

Doyle, S. H., Hubbard, B., Christoffersen, P., Young, T. J., Hofstede, C., Bougamont, M., ... Hubbard, A. (2018). Physical conditions of fast glacier flow: 1. Measurements from boreholes drilled to the bed of Store Glacier, West Greenland. *Journal of Geophysical Research: Earth Surface*, 123, 324–348. <https://doi.org/10.1002/2017JF004529>

Received 20 OCT 2017

Accepted 26 DEC 2017

Accepted article online 21 JAN 2018

Published online 24 FEB 2018

Physical Conditions of Fast Glacier Flow: 1. Measurements From Boreholes Drilled to the Bed of Store Glacier, West Greenland

S. H. Doyle¹ , B. Hubbard¹ , P. Christoffersen² , T. J. Young^{2,3} , C. Hofstede⁴ , M. Bougamont² , J. E. Box⁵ , and A. Hubbard⁶

¹Centre for Glaciology, Department of Geography and Earth Sciences, Aberystwyth University, Aberystwyth, UK, ²Scott Polar Research Institute, Cambridge University, Cambridge, UK, ³British Antarctic Survey, National Environmental Research Council, Cambridge, UK, ⁴Helmholtz Centre for Polar and Marine Research, Alfred Wegener Institute, Bremerhaven, Germany, ⁵Glaciology and Climate, Geological Survey of Denmark and Greenland, Copenhagen, Denmark, ⁶Centre for Arctic Gas Hydrate, Environment and Climate, Department of Geology, Arctic University of Norway, Tromsø, Norway

Abstract Marine-terminating outlet glaciers of the Greenland Ice Sheet make significant contributions to global sea level rise, yet the conditions that facilitate their fast flow remain poorly constrained owing to a paucity of data. We drilled and instrumented seven boreholes on Store Glacier, Greenland, to monitor subglacial water pressure, temperature, electrical conductivity, and turbidity along with englacial ice temperature and deformation. These observations were supplemented by surface velocity and meteorological measurements to gain insight into the conditions and mechanisms of fast glacier flow. Located 30 km from the calving front, each borehole drained rapidly on attaining ~600 m depth indicating a direct connection with an active subglacial hydrological system. Persistently high subglacial water pressures indicate low effective pressure (180–280 kPa), with small-amplitude variations correlated with notable peaks in surface velocity driven by the diurnal melt cycle and longer periods of melt and rainfall. The englacial deformation profile determined from borehole tilt measurements indicates that 63–71% of total ice motion occurred at the bed, with the remaining 29–37% predominantly attributed to enhanced deformation in the lowermost 50–100 m of the ice column. We interpret this lowermost 100 m to be formed of warmer, pre-Holocene ice overlying a thin (0–8 m) layer of temperate basal ice. Our observations are consistent with a spatially extensive and persistently inefficient subglacial drainage system that we hypothesize comprises drainage both at the ice-sediment interface and through subglacial sediments. This configuration has similarities to that interpreted beneath dynamically analogous Antarctic ice streams, Alaskan tidewater glaciers, and glaciers in surge.

Plain Language Summary Greenland's fast flowing tidewater glaciers account for significant contributions to sea level rise, yet little is known about the conditions within and beneath them. We instrumented boreholes drilled to the bed of Store Glacier with sensors to measure ice temperature and deformation, and subglacial water properties. These data reveal that the fast flow of Store Glacier is mainly caused by motion at the ice bed interface driven by highly pressurized subglacial water and basal sediments, together with a significant component of ice deformation concentrated in the lowermost 80 m of ice deposited in the last glacial period. The subglacial conditions, including inefficient subglacial drainage at high pressure, are similar to those observed beneath fast-flowing Antarctic ice streams, Alaskan tidewater glacier, and glaciers in surge.

1. Introduction

Over the last two decades the Greenland Ice Sheet (GrIS) has been the focus of considerable scientific attention due to its recent mass loss and the uncertainty regarding its future response to atmospheric and oceanic forcing. Despite major insights from satellite remote sensing (e.g., Howat & Eddy, 2011; Howat et al., 2010; Joughin, Howat, et al., 2008; Moon et al., 2014), glacio-oceanographic (Chauché et al., 2014; Motyka et al., 2011; Rignot et al., 2010; Straneo et al., 2010), and numerical modeling (e.g., Nick et al., 2013; Todd & Christoffersen, 2014; Xu et al., 2013) perspectives, Greenland's fast-flowing tidewater glaciers have been subject to relatively

©2018. The Authors.

This is an open access article under the terms of the Creative Commons Attribution License, which permits use, distribution and reproduction in any medium, provided the original work is properly cited.

few direct ground-based measurements (e.g., Iken et al., 1993; Nettles et al., 2008) due largely to the difficulty in accessing and operating in their environment. Our current understanding of tidewater glacier hydrology and mechanics has largely been informed by borehole-based measurements from glaciers in other regions of the world; notably Alaska (e.g., Kamb et al., 1994; Meier et al., 1994), although observations have been reported from calving glaciers in other regions, for example, from Patagonia (Sugiyama et al., 2011) and Svalbard (How et al., 2017; Vieli et al., 2004).

The fast flow of marine-terminating outlet glaciers is generally attributed to rapid basal motion, which relies upon a subglacial hydrological system sustained at high pressure over a large area of the bed to reduce friction and, where present, enhance the deformation of subglacial sediments (e.g., Kamb et al., 1994). These conditions are similar to those observed beneath ice streams and glaciers in surge (e.g., Engelhardt et al., 1990; Kamb et al., 1985), but direct evidence for subglacial material properties and conditions beneath fast-flowing marine-terminating glaciers remains limited (Humphrey et al., 1993; Walter et al., 2014). In Greenland, there is one exception: boreholes have been instrumented at four sites on Jakobshavn Isbræ (Iken et al., 1993; Funk et al., 1994; Lüthi et al., 2002, 2003). These studies revealed steeply curving temperature profiles with a minimum of -22°C near the center of the ice column, enhanced ice deformation rates below the Holocene-Wisconsin transition, and the presence of a basal temperate ice layer. From full-depth temperature profiles from sites located on the lateral margin of Jakobshavn Isbræ and extrapolated profiles from boreholes that did not reach the bed on the centerline, these studies inferred that vertical thickening of the basal temperate ice layer and more deformable Wisconsin ice plays an important role in the fast flow of this glacier. Several borehole-based investigations have also been conducted on slow-moving regions of the GrIS (i.e., those with an annual velocity of $\sim 100\text{ m yr}^{-1}$), including inland of marine-terminating Sermeq Avannarleq (e.g., Andrews et al., 2014; Ryser, 2014) and the land-terminating Kangerlussuaq sector (e.g., Meierbachtol et al., 2013; Smeets et al., 2012; Wright et al., 2016). These studies provided insight into the contrasting components of the subglacial hydrological system (e.g., Andrews et al., 2014) and the importance of stress distribution and transfer at the glacier bed (e.g., Ryser, Lüthi, Andrews, Hoffman, et al., 2014; Ryser, Lüthi, Andrews, Catania, et al., 2014). However, the issue of whether these studies' findings are representative of conditions beneath outlet glaciers flowing several time faster remains to be answered.

Furthermore, relative to its size and spatial heterogeneity, there is a notable paucity of ice temperature measurements from the ablation area of the GrIS and, in particular, from fast-flowing tidewater outlet glaciers. Two temperature profiles to 50% of the ice thickness were obtained at Jakobshavn Isbræ's centerline, with two further full-depth profiles from adjacent sites (Iken et al., 1993; Lüthi et al., 2002). An additional five temperature profiles have been reported from sites in the Paakitsoq area (Thomsen et al., 1991), and two from sites on Sermeq Avannarleq (Lüthi et al., 2015; Ryser, 2014). Farther south, temperature profiles have been published for five sites on Russell Glacier (Harrington et al., 2015). Hence, of the total inventory of seventeen temperature profiles documented across the entire ablation area of the GrIS, only two are full-depth profiles from a fast-flowing tidewater outlet glacier, and these are from its shear margins.

Extending our knowledge of the temperature structure, deformation profile, and basal conditions of Greenland's marine-terminating outlet glaciers is critical to furthering our understanding of the mechanics of their fast flow and for accurately parameterizing their behavior in numerical ice sheet models. To this end, here we present findings from a suite of boreholes drilled to the bed of Store Glacier, a fast-flowing tidewater outlet glacier that drains the western sector of the GrIS. The drill site was deliberately located on the main centerline of Store Glacier, where surface velocities are $> 1.5\text{ m d}^{-1}$, specifically to allow us to investigate the subglacial and englacial conditions associated with the mechanics of fast glacier flow.

2. Field Site

Store Glacier (*Qarassap Sermia*) is the third fastest outlet glacier in West Greenland and one of its largest, draining a catchment area of $\sim 34,000\text{ km}^2$ (Rignot et al., 2008). The glacier discharges into Uummannaq Bay at 70°N , where its 5.2 km wide calving front is heavily crevassed with large, unstable seracs characteristic of fast flow (Figure 1). In contrast with the majority of Greenlandic outlet glaciers, which have thinned and retreated over the last two decades, the terminus of Store Glacier has remained in a similar position since at least 1948 (Weidick, 1995), and the lowermost 10 km section thickened by 10–15 m between 2004 and 2012 (Csatho et al., 2014). Centerline flow speeds at the terminus vary depending on the measurement period, with estimates ranging from 4 to 7 km yr^{-1} , equivalent to 11–18 m d^{-1} (Ahn & Box, 2010; Joughin et al., 2011;

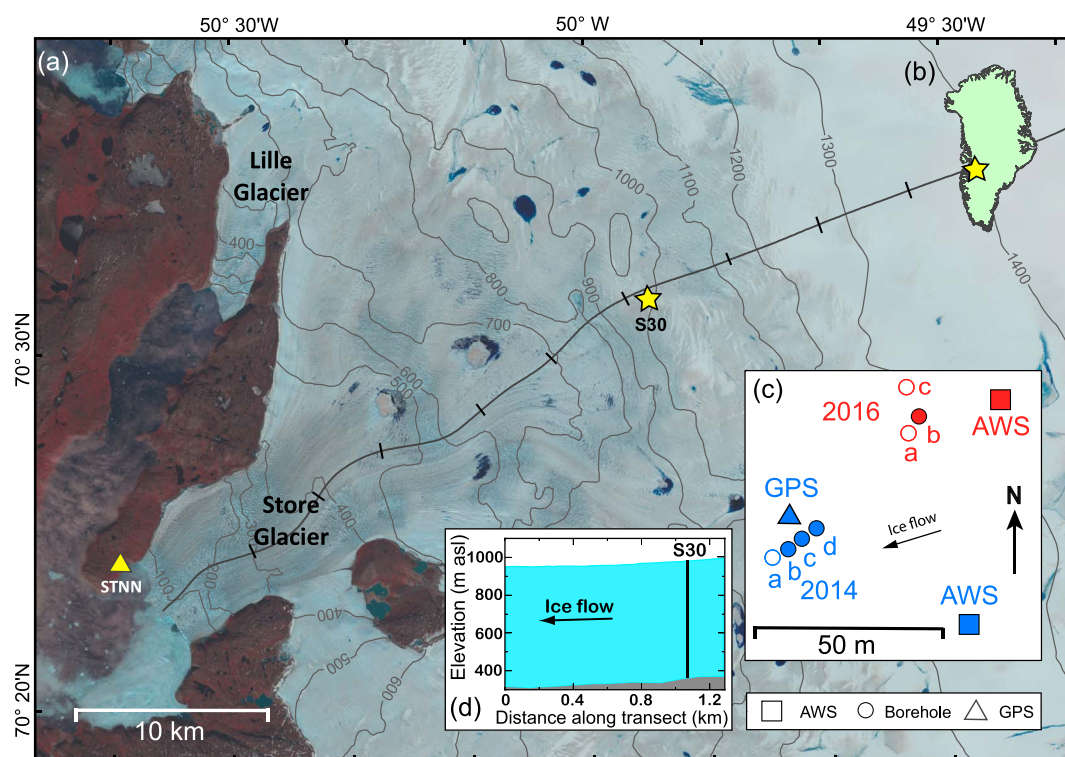


Figure 1. (a) Map showing the location of the field site, S30, on Store Glacier with insets showing (b) the location in Greenland, (c) a close up of S30, and (d) a flow-parallel ice surface and bedrock elevation profile surveyed using GPS and phase-sensitive radar. The background on Figure 1a is a Landsat 8 image acquired on 1 July 2014, and the elevation contours are derived from Howat et al. (2014). The central flowline marked on Figure 1a with a black line is ticked every 5 km from the terminus. On Figure 1c boreholes are color coded by year with uninstrumented boreholes shown as unfilled circles.

Ryan et al., 2014). Upglacier, surface velocities decrease to $\sim 1 \text{ km yr}^{-1}$ at 16 km from the terminus (Walter et al., 2012), and $\sim 600 \text{ m yr}^{-1}$ at 30 km from the terminus (Joughin, Das, et al., 2008).

A reconnaissance of potential drill sites was made in early May 2014, and a site located close to the central flowline, 30 km from the terminus was selected, hereafter named S30 ($N70^{\circ}31'$, $W49^{\circ}55'$, 982 m above sea level (asl); Figure 1). Global positioning system (GPS) receivers and an automated weather station (AWS) were deployed and an ice thickness survey was conducted using phase-sensitive radar (e.g., Brennan et al., 2014; Young et al., 2016). Ice thickness at S30 was determined to be $\sim 600 \text{ m}$, and between 12 May and 14 July 2014 the surface velocity averaged 608 m yr^{-1} in the WSW direction 253° . The mean surface slope in the flow direction was estimated to be 2.3° by applying linear regression to a surface elevation profile 10 ice thicknesses in length, centered on the drill site, and sampled from the 30 m resolution digital elevation model of Howat et al. (2014). The site is bounded on all sides by major crevasse fields—a characteristic of much of Store Glacier's lower 40 km outlet tongue, but particularly toward the calving front. The drill site was located within an area of water-filled crevasses, with open crevasses and small ($< 2 \text{ m}$ diameter) moulins located $\sim 1 \text{ km}$ to the west. Ice flow from the vicinity of the drill site advects directly into an icefall, located $\sim 2 \text{ km}$ to the west.

3. Methods

3.1. Hot Water Drilling and Instrumentation

In late July and early August 2014, four adjacent boreholes were drilled to the bed at S30 within a 10 m^2 area using a hot water drilling system. An additional three boreholes were drilled to the bed in July 2016 at a site located 50 m to the northeast of the 2014 drill site (Figure 1). Each borehole (BH) is named by the two-digit year and a letter, with, for example, BH14a indicating the first borehole drilled in 2014 (Figure 2 and Table S1 in the supporting information).

The drill system was similar to that described by Makinson and Anker (2014): Three pressure-heater units (Kärcher HDS 1000 DE) delivered a total of 45 l min^{-1} of water at $70\text{--}80^{\circ}\text{C}$ and 11 MPa to a 2.1 m long drill stem

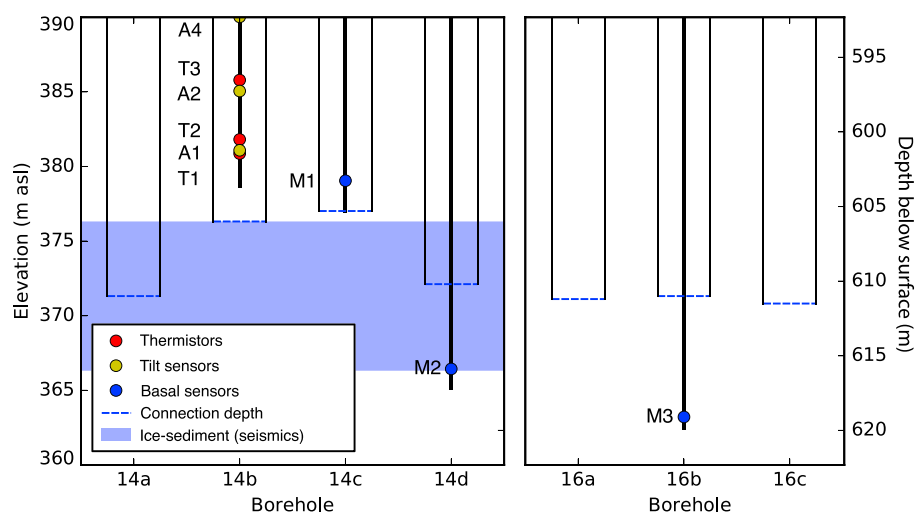


Figure 2. Diagram showing depth estimates of (i) sensors near the ice-sediment interface; and (ii) the breakthrough depth of each borehole's connection to the subglacial drainage system. The blue shade represents the range in the best estimates of the ice-sediment interface from seismic reflection, as measured in July 2014 (Hofstede et al., 2018). The surface elevation was surveyed using GPS at 982.3 m asl. The basal sensors (M1, M2, and M3) measured pressure, temperature, and EC, and M3 made additional turbidity measurements.

through a 1,000 m long, 19 mm (0.75") hose. To detect the glacier bed and measure the depth of the drill, we recorded the length and weight of spooled-out hose using a rotary encoder and load cell located on a sheave wheel on the drilling rig at a 2 s interval (e.g., Figures S1 and S2). The drill's progress was governed by a mechanical winch. Due to low englacial temperatures, relatively large diameter boreholes (>0.15 m diameter at the surface) were drilled to allow sensors, which were connected via multicore cables, to be installed before the boreholes refroze. Indeed, installation of a thermistor string in BH14a failed for this reason. To overcome this problem, subsequent boreholes were drilled at a slower rate with a wider-angled, solid-cone water jet (Table S1). In 2014, we drilled at a mean rate of 1.2 m min^{-1} allowing 600 m long boreholes with an initial estimated diameter of $\sim 0.15 \text{ m}$ to be completed within 8.5 h (Table S1). Following drilling, it took $\sim 1.25 \text{ h}$ to recover the drill from the bed and, with the exception of BH14a, we continued to deliver hot water to the drill while it was raised to delay borehole refreezing. In 2016, we drilled at slower mean rates of 1.0 m min^{-1} (BH16a) and 0.5 m min^{-1} (BH16c) to similar depths, achieving slightly larger borehole diameters (e.g., 0.2 m for BH16c) in $\sim 10 \text{ h}$ and $\sim 20 \text{ h}$, respectively (Table S1).

For BH14a, BH14b, BH14c, BH16a, and BH16b the drill was reversed almost immediately after connection with the subglacial hydrological system was made (e.g., see Figure S1). For BH14d, extra effort was made to ensure that the multisensor unit was installed at the bed, and contact with the substrate was assumed when the progress became slower and more hesitant; however, drill lowering did not cease completely. Extended drilling efforts were also made to allow (unsuccessful) attempts to recover sediment cores from BH16c. BH16c connected and drained at 611.5 m depth, below which drilling progressed intermittently at a slower (averaging 0.4 m min^{-1}) and more variable rate, including transient periods of partial unloading (Figure S2). At 657 m depth the drill's progress ceased completely, which we interpret as indicating contact with bedrock or consolidated sediments. The drill was then recovered to the surface and a sediment corer was lowered to the bed, but no sediment was retrieved. A further attempt to take a sediment core resulted in the corer becoming irretrievably lodged in the borehole.

The remaining three 2014 boreholes were successfully instrumented with a range of englacial and basal sensors (Figure 2). A string of 11 thermistors (T1 to T11) and five analog tilt sensors (A1 to A5) were installed in BH14b, and two multisensor units (M1 and M2), which measure pressure, temperature, and electrical conductivity (EC), were installed at the base of BH14c and BH14d. In 2016 a multisensor unit (M3), equipped with an additional turbidity sensor, was installed at the base of BH16b. Installation depths of the sensors were estimated from markings on the cable and from the water pressure recorded by the pressure sensors (Figure 2 and Table S1).

Analog data from the borehole sensors were digitized at the surface using Campbell Scientific CR1000 data loggers powered by a 12 V, 36 Ah battery and a 5 W solar panel. During sensor installation, measurements were logged at a high sampling rate (4 s in 2014; 5 s in 2016) to enable EC profiling (Figure S6) and detection of the water level below the surface. Following installation in 2014, data were recorded at a 10 min interval during the field campaign and hourly thereafter. In 2016 these sampling intervals were reduced to 1 min and 30 min, respectively. Data are presented at the raw time interval unless otherwise stated. The records from 2014 began on 26 July 2014 and span from 28 to 334 days, with sensors located deeper than ~550 m below the surface failing or becoming redundant due to cable rupture or freezing in (Table S2). Hence, the 2014 data sets span the transitional period between late summer and winter. Data from 2016 were acquired from 12–24 July 2016 and therefore only cover summer conditions.

The borehole data sets are supplemented by contemporaneous measurements of surface ice motion and meteorological variables made by the GPS receivers and AWS deployed at S30 (Figure 1).

3.2. Temperature Measurements

The vertical temperature profile at the drill site was constrained by 11 thermistors in BH14b (T1 at 601.5 m depth to T11 at 101.7 m depth), and two thermistors incorporated into the basal pressure sensors: M1 at 603.3 m depth in BH14c, and M2 at 615.9 m depth in BH14d (Tables S2 and S3). Temperature data from M3 are not presented as the thermistor was not calibrated. The thermistor string consisted of 11 negative temperature coefficient thermistors (Fenwell UNI-curve 192-502-LET-AOI) unequally spaced to achieve a greater density of measurements near the bed (Table S3). Thermistor resistance, measured using a half bridge relative to a precision reference resistor, was converted to temperature by fitting a Steinhart and Hart (1968) polynomial to the manufacturer's calibration and subtracting an individual "freezing point offset" obtained from an ice bath calibration. Previous studies (Bayley, 2007; Iken et al., 1993) indicate that an uncertainty of $\pm 0.05^\circ\text{C}$ for temperatures near 0°C can be achieved using this technique. Three of the thermistors installed at or near the bed (T1, M2, and M3) did not freeze in and therefore did not record an ice temperature (Figure 4). For the remaining thermistors, the undisturbed ice temperature (T_0) was estimated by extrapolating the temperature curve during the postfreezing equilibration phase of cooling. Following Humphrey and Echelmeyer (1990) and Ryser (2014) the temperature T in the borehole at time t is given by

$$T(t) = \left(\frac{Q}{4\pi k(t-s)} \right) + T_0, \quad (1)$$

where Q is the heat released per unit length of the borehole during drilling, $k = 2.1 \text{ W m}^{-1} \text{ K}^{-1}$ is the thermal conductivity of ice, T_0 is the undisturbed ice temperature, and s is the delay in seconds until the onset of asymptotic cooling. Following Ryser (2014), the parameters Q , s , and T_0 were determined by fitting equation (1) to the temperature time series during the equilibration phase of cooling. The estimates of T_0 were up to 160 mK below the final recorded temperature, but typically less than 60 mK below (Table S3). A period of warming recorded at T3 with a temperature increase of 0.06°C had to be excluded from the curve fitting (Figure 4). We also excluded T1 and M2 from the ice temperature profiles as they never froze in.

3.3. Water Pressure Measurements

Water pressure at the base of BH14c, BH14d, and BH16b was measured using three Geokon 4500SH vibrating wire piezometers (M1, M2, and M3; Figure 2) calibrated by the manufacturer to an accuracy of $\pm 1.22 \text{ kPa}$ ($\pm 0.12 \text{ mH}_2\text{O}$). Water pressure was corrected for the different installation depths of the sensors to a reference depth of 611 m below the ice surface. Temperature was measured using the piezometers' internal thermistor; the manufacturer's calibration of which was improved by further calibration in an ice bath with the thermistor string. As the boreholes refroze rapidly we assume that the pressure measurements were not influenced by either atmospheric pressure variations or water entering the borehole from the surface, as sometimes occurs on temperate glaciers (e.g., Gordon et al., 2001). The water level below the surface in each borehole was measured immediately postbreakthrough relative to accurately taped distance markers on the cable while detecting the water surface with the pressure and EC sensors (Table S1).

3.4. Electrical Conductivity Measurements

The EC of water is proportional to the concentration of dissolved ions and can be used as a proxy for dissolved solids (Fenn, 1987). EC was determined by inverting the resistance measured across two brass-rod electrodes (5 mm diameter; 11 mm long, 11 mm separation; e.g., Stone et al., 1993). The resistance across the electrodes was measured at the surface using a half bridge relative to a precision reference resistor. To cancel polarization

Table 1

Depth, Interpolated Undisturbed Ice Temperature T_0 , Tilt Rate, and the Vertical Gradient of Horizontal Velocity for Each Tilt Sensor Installed in BH14b

Sensor	Depth m	T_0 °C	$T_m(\gamma_{\text{air}})$ °C	$T_m(\gamma_{\text{pure}})$ °C	$d\theta/dt$ °d ⁻¹	du/dZ	
						Data year ⁻¹	Theory
A1	601.2	-0.71	-0.510	-0.384	-0.017	0.106	1.305
A3	592.3	1.12	-0.502	-0.378	+0.254	1.725	1.157
A4	552.5	-5.87	-0.468	-0.352	+0.232	1.554	0.387
A5	401.9	-18.87	-0.337	-0.253	+0.029	0.182	0.026

Note. Negative tilt rates indicate that the sensor was initially installed inclining away from the direction of tilt. Tilt sensor A2 at 597.3 m depth did not operate correctly and is not listed.

effects, the polarity of the excitation voltage was reversed. The EC sensors were calibrated in sodium chloride solutions against a laboratory EC probe.

EC sensors were installed at the base of BH14c, BH14d, and BH16b and EC depth profiles were obtained from BH14c and BH14d shortly after drilling (Figure S6; supporting information S1, section 2.1).

3.5. Turbidity Measurements

The turbidity sensors were adapted from a design detailed in Orwin and Smart (2005). They use a photo diode to measure the backscatter of infrared (IR) light emitted by an IR light emitting diode (LED). Higher suspended sediment concentrations (SSCs) result in greater backscatter up to a certain SSC limit, beyond which insufficient light is transmitted through the water. The photo diode and LED were mounted with a focal length of 5 cm, and potted in clear urethane resin. The sensors first take an ambient measurement with the LED off, and this reading (found to be almost constant at 5–6 mV when not exposed to ambient light) is subtracted from the reading with the LED on.

The absolute calibration of turbidity sensors is complicated by their sensitivity to lithology and grain size and it is common for studies measuring proglacial river turbidity to calibrate against SSCs derived from in situ water samples (e.g., Bartholomew et al., 2011; Orwin & Smart, 2004). For this reason previous studies have reported subglacial turbidity measured in boreholes in relative units (e.g., Gordon et al., 2001; Stone & Clarke, 1996; Stone et al., 1993). In this study, we adopted an intermediate approach by laboratory calibration using nonlocal, fine (grain size <63 μm) glacial sediment using SSCs ranging from 0 g l⁻¹ (distilled water) to 8 g l⁻¹ sampled from west Wales, UK. The calibration was approximately linear between 0 and 3 g l⁻¹ with the sensor output varying from 56 mV in distilled water to ~300 mV in 3 g l⁻¹ (Figure S7a). Above concentrations of 3 g l⁻¹ (not shown) it was difficult to keep sediment suspended in the laboratory even using mechanical stirring devices. Higher SSCs, at least up to ~20 g l⁻¹, have been reported for turbulent waters emerging at the ice sheet margin and in proglacial rivers (e.g., Bartholomew et al., 2011; Hasholt et al., 2013). Despite the limitations of the calibration noted above, we expect SSCs between 3 and 20 g l⁻¹ to fall within the full scale range of our sensor, which was set at 800 mV using a white reflector.

3.6. Ice Deformation Measurements

Borehole tilt was recorded by five three-axis analog microelectromechanical system (MEMS) accelerometers (Model: MMA7361) installed at depths of 601.2, 597.3, 592.3, 552.3, and 401.9 m below the surface in BH14b, with a higher sampling density toward the bed (Table 1). The voltage output of the accelerometers was digitized at the surface by a Campbell CR1000 data logger. The tilt sensors are numbered A1 to A5 upward from the lowermost sensor (Table 1). With the exception of A2, all the tilt sensors operated continuously between 26 July and 29 September 2014 (Table S2).

The sensors were installed so that the z axis initially recorded approximately 1g when hanging vertically in the borehole. Assuming that the only measured acceleration was due to gravity, the sensors' roll (α) and pitch (β) were calculated from the acceleration (a) measured along the x, y, and z axes fixed to the sensors' body relative to gravity:

$$\alpha = \tan^{-1} \left(\frac{a_y}{\sqrt{a_x^2 + a_z^2}} \right), \quad (2)$$

$$\beta = \tan^{-1} \left(\frac{a_x}{\sqrt{a_y^2 + a_z^2}} \right). \quad (3)$$

Although it is possible to calculate tilt using just one or two of the axes, due to the derivative of the sine function, this results in a lower sensitivity to tilt angle when the sensing axis is close to vertical. To correct for this, equations (2) and (3) above use readings from all three axes to ensure constant sensitivity to tilt angle over the full 360° of rotation.

The manufacturer's stated resolution of the tilt sensors of 800 mV g^{-1} (where g is the normalized gravity vector) is equivalent to 8.9 mV per degree of tilt. As there are additional uncertainties caused by the voltage transmission and digitization, we estimated the precision from the noise level in the voltage readings by calculating the standard deviation of the linearly detrended voltage time series during a period of steady tilt. For the uppermost sensor A5 between 29 August and 29 September 2014, and after removing anomalies where the resultant acceleration $a \neq 1g$ (discussed below), the resulting estimate of precision averaged across all three axes is ± 2.3 mV. This is equivalent to a tilt angle precision of $\pm 0.26^\circ$. The absolute accuracy of the tilt sensors was determined to be less than $\pm 1^\circ$ using a rotary table which was itself limited to graduations of 1° .

As sensor azimuth was not measured, the sensors were assumed to tilt in the direction of ice flow, and α and β were resolved to single-axis tilt denoted θ :

$$\theta = \cos^{-1} (\cos \alpha \cos \beta). \quad (4)$$

When interpreting tilt measurements made in this way, it is important to consider that the sensors may not be installed precisely vertically in the borehole: sensors that are initially inclined away from the direction of tilt may therefore measure a reduction in tilt angle through time until the sensor passes through vertical (see, e.g., Figure S4d). If the sensor is not stationary during the measurement period, that is, the sensor also measures acceleration other than that due to gravity, the root-mean-square sum of the accelerations measured on the x , y , and z axes may not be equal to $1g$. Although recording such accelerations could compromise the calculation of tilt at short timescales, it has the advantage that the sensors may be capable of discerning transient accelerations (e.g., due to icequakes or brittle fracture).

We inferred the vertical gradients of horizontal velocity du/dz at each tilt sensor following a method described by Ryser, Lüthi, Andrews, Hoffman, et al. (2014) and references therein. We first estimated the mean tilt rate at each sensor by applying linear regression to the tilt time series during a period (3–26 September 2014) of steady surface ice motion and englacial tilt (Figure S4 and Table 1). Prior to linear regression, data were removed from the analysis if the resultant acceleration (a) did not equal $1g$ (Figure S4). The vertical gradients of horizontal velocity were estimated as

$$\frac{du}{dz} = \frac{\tan \theta_1 - \tan \theta_0}{\Delta t}, \quad (5)$$

where θ at times t_1 and t_0 was calculated from the tilt rate and $\Delta t = t_1 - t_0$. The profile of horizontal velocity due to deformation u_d was determined by integrating cumulatively the measured values of du/dz with respect to depth (Figure 5c). Following previous analyses (Lüthi et al., 2002; Ryser, Lüthi, Andrews, Hoffman, et al., 2014), we compared our estimates of du/dz and u_d determined from the tilt measurements with those expected from theory. Assuming a gravity-driven parallel-sided slab of ice at inclination angle ϕ ,

$$\frac{du}{dz} = 2A(\rho_i g h \sin \phi)^n, \quad (6)$$

where A (in units of $s^{-1} Pa^{-3}$) is the rate factor in Glen's flow law, $\rho_i = 900 \text{ kg m}^{-3}$ is the ice density, $g = 9.81 \text{ m s}^{-2}$ is gravitational acceleration, $h = 611 \text{ m}$ is the height of the overlying ice column, and $n = 3$ is a unitless power law exponent (e.g., Glen, 1955; Nye, 1957). Values of the rate factor A were determined for the temperature profile (Figure 5a) based on those published in Cuffey and Paterson (2010), which were found by Ryser, Lüthi, Andrews, Hoffman, et al. (2014) to closely match similar borehole-based tilt measurements on Sermeq Avannarq. The inclination angle ϕ was prescribed as the mean surface slope (see section 2).

Measuring borehole tilt at only four depths of a 611 m deep ice column results in a large uncertainty in the integrated deformational velocity, especially where gradients in horizontal velocity are steep. In an attempt to address this we also applied an alternative interpolation to the measured horizontal velocity gradients assuming a sharp increase in deformation rates at 528 m depth, which corresponds to the inferred depth of the Holocene-Wisconsin transition (HWT), discussed in section 5.3 (Figure 5b). The assumption that deformation rates increase markedly below the HWT is consistent with measurements from site GULL on Sermeq Avannarleq (Ryser, Lüthi, Andrews, Hoffman, et al., 2014) and site D on Jakobshavn Isbræ (Lüthi et al., 2002), as well as the mechanical properties of ice age ice (e.g., Paterson, 1991).

Basal motion u_b was then estimated for each profile by subtracting the depth-integrated deformational velocity u_d from the mean surface velocity u_s measured by GPS during this period of 591.8 m yr⁻¹:

$$u_b = u_s - u_d. \quad (7)$$

3.7. Ice Surface Motion Measurements

Horizontal ice surface velocity and vertical surface height were derived from GPS measurements. In 2014, the GPS receiver was located ~5 m from the drill site, and it is this position that is shown on Figure 1c. In 2016, the GPS receiver was located ~600 m to the west of the drill site where mean ice velocity was higher. GPS antennae were installed on 4.9 m long poles drilled 3.9 m into the ice surface. Dual-frequency Trimble 5700 and R7 receivers operated continuously, sampling at a 10 s interval. The GPS receivers were powered by a 50–100 Ah battery, solar panels, and a wind generator, yet some data gaps occurred due to power outage. Data from the receivers were processed kinematically (King, 2004) using Track v 1.28 (Chen, 1998) relative to bedrock-mounted reference receivers using the final precise ephemeris from the International GNSS Service (Dow et al., 2009), and IONEX maps of the ionosphere (Schaer et al., 1998). A reference GPS receiver was located on bedrock near the glacier terminus (STNN) giving a baseline length of 30 km (Figure 1). GPS measurements of surface ice motion are presented as horizontal velocity and linearly detrended vertical displacement and are filtered with a low-pass Butterworth filter with a cutoff frequency equivalent to a period of 12 h. We present linearly detrended vertical displacement in an attempt to isolate periods of uplift caused by hydraulic ice bed separation from vertical motion caused by sliding along an inclined bed. We note, however, that some vertical motion may also result from vertical strain (e.g., Sugiyama & Gudmundsson, 2003), which we have not corrected for. Assuming steady ice motion, uncertainties in the positions were estimated at <2 cm in the horizontal and <5 cm in the vertical by examining the linearly detrended position time series between 5 and 10 September 2014.

3.8. Meteorological Measurements

The AWS recorded a comprehensive range of meteorological variables (see, e.g., van As, 2011) but only near-surface (2–3 m above the surface) air temperature, relative humidity, and ice melt rate are presented here. Surface height change measured by a Campbell Scientific SR50 sonic ranger was converted to a water equivalent (we) ice melt rate assuming an ice density of 900 kg m⁻³. The AWS sampled at a 10 min interval and data are presented as hourly averages.

Daily precipitation totals for the vicinity from NCEP/NCAR reanalysis data (Kalnay et al., 1996) are also presented. The timing of precipitation at the drill site can be confirmed from the relative humidity measurements, as a relative humidity of >95% is a reliable indicator of either fog or rainfall. These time series are augmented by synoptic tracking of the associated weather systems using daily maps of the atmospheric pressure at sea level (Movies S9 and S10).

4. Results

4.1. Drilling Observations

The water level in all seven boreholes dropped rapidly to ~80–90 m below the surface when the drill stem attained a recorded depth of 605.3–611.5 m (Movie S8). Rapid borehole drainage, hereafter termed breakthrough, was measured indirectly as an increase in load caused by frictional drag on the drill hose, indicating that the boreholes drained in 118–210 s (Figure 3 and Table S1). Given postdrainage water levels of ~80 m below the ice surface and assuming a uniform borehole diameter of ~0.15 m, a mean drainage rate of 0.012 m³ s⁻¹ is estimated for the breakthrough of both BH14c and BH14d (Table S1). It is pertinent that the first boreholes drilled to the bed in each year took longer to drain and had a broader load-time curve than

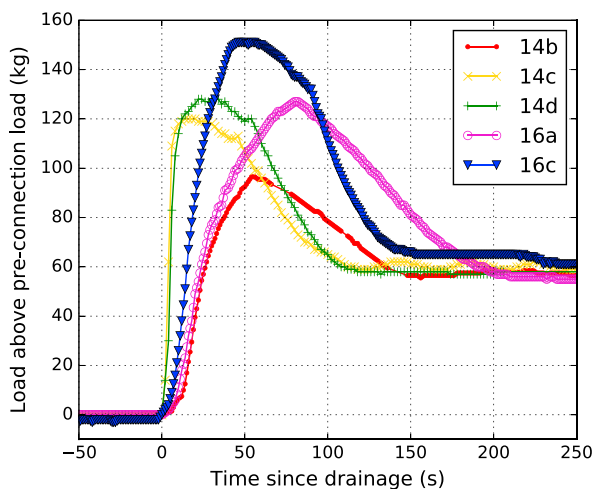


Figure 3. Load on the drill tower caused by frictional drag on the hose during the breakthrough of boreholes to the subglacial drainage system as a proxy for the borehole drainage rate. The offset between the pre-drainage and post-drainage load can be explained by the greater weight of the hose in air than in water after the borehole had drained to ~80–90 m below the surface.

subsequent boreholes. For example, with a drainage time of 210 s, BH16a took 57 s (37%) longer to drain than neighboring BH16c, which drained in 153 s (Figure 3 and Table S1). The breakthrough of subsequent boreholes also resulted in pressure, temperature and EC perturbations in existing boreholes. For example, as BH14d connected to the bed and drained, an asymmetric pressure impulse was recorded by the piezometer in neighboring BH14c, which was separated by 7 m at the surface (Figure S3a). The pressure in BH14c almost immediately, and rapidly, increased by 0.12 MPa in ~100 s and then gradually decayed, returning to preceding values over ~17 h. Corresponding spikes in EC and basal temperature in BH14c were also measured at this time (Figures S3b and S3c). Temperature perturbations were also recorded by thermistors near the base of BH14b following the breakthroughs of both BH14c and BH14d (Figure 4). All of these observations confirm that each and every borehole we drilled connected and interacted with the subglacial hydrological system.

4.2. Ice Temperature

The ice temperature profile exhibits a steep curve characteristic of fast ice flow with the minimum of $-21.25 \pm 0.05^\circ\text{C}$ at 302 m depth, almost exactly midway between the surface and the bed (Figure 5a and Table S3). A distinct kink in the temperature profile is apparent between 302 and 451 m below the surface, with temperatures at T8, located 401.9 m below the surface, ~1 to 2°C higher than would be expected by interpolating the curve with T8 omitted. With the

exception of T1, M2, and M3, the recorded temperatures fell below the melting-point temperature T_m adjusted for pressure (Table S3):

$$T_m = T_{tr} - \gamma(p_i - p_{tr}), \tag{8}$$

where γ is the Clausius-Clapeyron constant, $T_{tr} = 273.16\text{ K}$ and $p_{tr} = 611.73\text{ Pa}$ are the triple point temperature and pressure of water respectively, and p_i is the ice overburden pressure. For an inclined, parallel-sided slab of ice p_i can be approximated as

$$p_i = \rho_i g h \cos \phi, \tag{9}$$

where $\rho_i = 900\text{ kg m}^{-3}$ is the density of ice, $g = 9.81\text{ m s}^{-2}$ is gravitational acceleration, h is the height of the overlying ice column, and $\phi = 2.3^\circ$ is the mean surface and bed slope (see section 2). Typical end-member values of the Clausius-Clapeyron gradient range from $\gamma_{\text{pure}} = 0.0742\text{ K MPa}^{-1}$ for pure ice and air-free water (e.g., Cuffey & Paterson, 2010) to $\gamma_{\text{air}} = 0.0980\text{ K MPa}^{-1}$ for pure ice and air saturated water (Harrison, 1972).

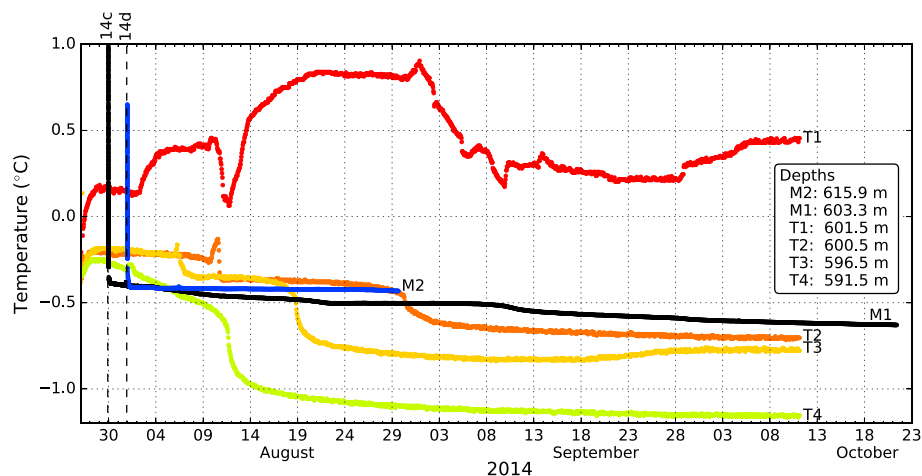


Figure 4. Temperature-time series for the thermistors near the bed in BH14b (T1 to T4), BH14c (M1), and BH14d (M2). The two dashed vertical lines show the timing of the connection of BH14c and BH14d to the subglacial hydrological system.

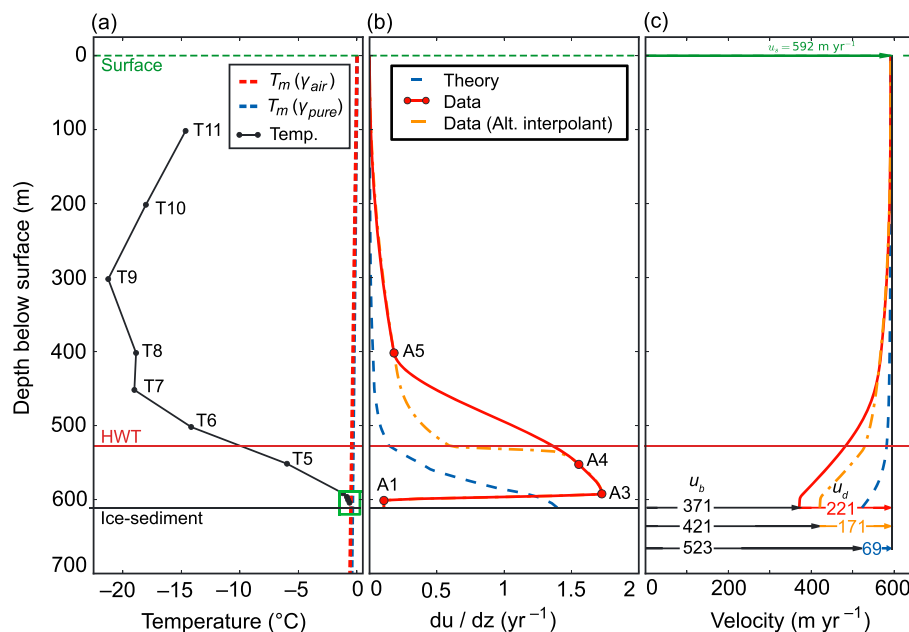


Figure 5. Depth profiles of (a) temperature, (b) internal deformation, and (c) velocity at site S30. The red dashed line on Figure 5a is the Clausius-Clapeyron gradient for pure ice and air-saturated water, and the green box around the ice-sediment interface shows the extent of Figure 6. An alternative interpolant is plotted on Figure 5b with an orange dashed line. Theoretical horizontal velocity gradients du/dz and deformational velocities (blue dashed lines) plotted on Figures 5b and 5c were calculated using Glen’s flow law and the surface slope. See text for details.

An intermediate value of 0.079 KMPa^{-1} was estimated by Lüthi et al. (2002) from ice temperature measurements on Jakobshavn Isbræ, indicative of a low content of soluble impurities and air within the ice. In section 5.2, we explore how the range of possible Clausius-Clapeyron constants influences our interpretation of the thermal regime and, in particular, the thickness of basal temperate ice.

The estimated undisturbed ice temperature (T_0) for the deepest thermistor which froze in, M1 in BH14c, of -0.64°C is 0.1 to 0.3°C below T_m assuming Clausius-Clapeyron constants for air-saturated and pure water, respectively (Table S3). M1 therefore extends the linear trend in temperature with depth from thermistors T2 and T3 installed in BH14b (Figure 6). As none of the thermistors were installed directly in temperate basal ice (Table S3), it is not possible to constrain precisely the depth of the theoretical transition surface between cold and temperate ice (CTS). Instead, the depth range of the CTS can be constrained from the intersection of the Clausius-Clapeyron gradient and the linear extrapolation of the temperature gradient for the lowest three thermistors that froze in, using both end-member Clausius-Clapeyron constants (Figure 6). Incorporating a thermistor depth uncertainty of ± 2 m, we constrain the CTS depth at $606.6\text{--}614.7$ m below the surface. Using the Clausius-Clapeyron constant determined for a site on Jakobshavn Isbræ by Lüthi et al. (2002) of 0.079 KMPa^{-1} gives a CTS depth of 612.1 m below the surface.

Thermistor T1, installed at a depth of 601.5 m in BH14b, recorded temperatures above T_m for 76 days with notable episodes of warming and cooling, which contrast markedly with the characteristic freezing curve present in all the other records (Figure 4). The temperature recorded by T1 increased from -0.28°C at installation and stabilized at $+0.17^\circ\text{C}$ before increasing again on 2 August to $+0.40^\circ\text{C}$ (Figure 4). A brief dip down to $+0.06^\circ\text{C}$ interrupted a trend of continued warming, which peaked at $+0.88^\circ\text{C}$ on 31 August. T1 then cooled and thereafter varied between $+0.15^\circ\text{C}$ and $+0.45^\circ\text{C}$.

Although we cannot rule out the possibility that thermistor T1, which remained substantially above the melting-point temperature (Figure 4), was not working or calibrated incorrectly, there are three lines of evidence that suggest otherwise: (i) the thermistor ice bath calibration curve for T1 was consistent with that of all the other thermistors; (ii) the temperature time series for T1 does not show the characteristic freezing curve observed for all the other thermistors, which suggests that the thermistor did not freeze in; and (iii) damage to the thermistor cable caused by deformation or basal sliding would be likely to stretch the cables which would increase its resistance and drive apparent temperature downward, not upward.

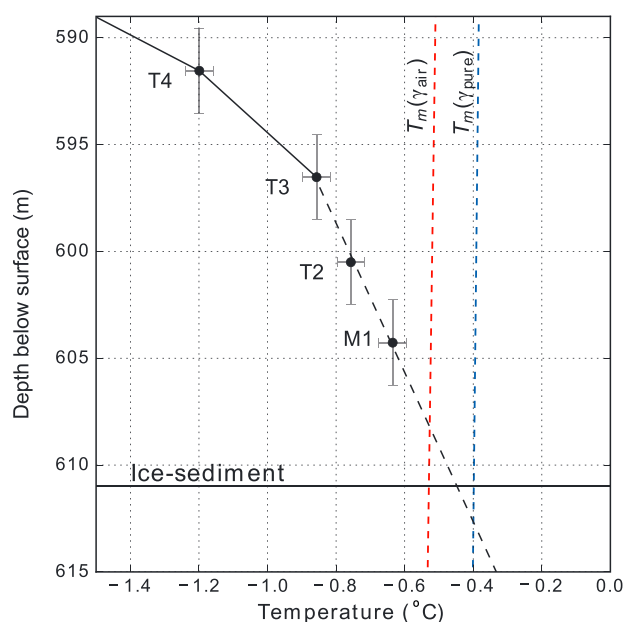


Figure 6. Ice temperature-depth profile for thermistors near the inferred ice-sediment interface. The line of linear regression for the lowest three thermistors is shown with a black dashed line. The subvertical blue and red dashed lines show the melting temperature assuming Clausius-Clapeyron constants for pure ice and pure water and pure ice and air saturated water, respectively.

Transient perturbations in temperature at T1 do, however, appear coincident with variations recorded by adjacent thermistors (e.g., with T2 on 10 August). For instance, it is possible that the increase in T1 temperature coincident with the thermal arrest and freezing of T2 (represented by steady temperatures followed by the characteristic freezing curve) was caused by the latent heat released by adjacent water freezing. It is notable that the temperature at T1 decreased sharply once T2 had completely frozen in (i.e., after the period of thermal arrest; Figure 4). Furthermore, the sharp peak in T2 temperature coincident with the $+0.06^{\circ}\text{C}$ nadir of T1 prior to the beginning of thermal arrest at T2 could represent the input of water at a temperature between that of T2 and T1 (Figure 4). Although the latent heat released by adjacent ice freezing appears coincident with the timing of T1 temperature variations it is difficult to accept this as an explanation for the high water temperatures measured by T1.

The temperature recorded by M2 also never fell below T_m , possibly due to insufficient time to equilibrate in its 29 days of operation. Nevertheless, with a mean temperature of -0.42°C from 8 to 29 August the temperature recorded by M2 was substantially lower than that of T1 and more consistent with the other thermistor measurements (Figure 4).

Overall, thermistors installed below 550 m depth stopped working after 76 to 93 days while thermistors above 550 m depth continued to operate correctly for at least 343 days (Table S2). Some of the continuous records did, however, suffer from discrete, usually negative, jumps in temperature consistent with increases in cable resistance with episodic cable strain. These jumps were particularly evident at T6 at 501.94 m depth and were coincident with the failure

of lower thermistors. The deepest thermistor in BH14b, T1, failed first after 76 days, while thermistors T2 to T5 failed after 78–93 days, and not strictly in depth order.

4.3. Borehole Tilt and Ice Deformation

Enhanced deformation rates were measured at sensors A4 and A3 at 552.5 and 592.3 m below the surface, with lower deformation rates measured by A5 (401.9 m depth) and by A1 near the bed (601.2 m depth; Figure 5b; Table 1). Subtracting the depth-integrated deformational velocity, $u_d = 220 \text{ m yr}^{-1}$, from the surface velocity, $u_s = 592 \text{ m yr}^{-1}$, we estimate that basal motion, u_b , averaged 372 m yr^{-1} between 3 and 26 September 2014. Hence, basal motion accounted for 63% of surface motion during this period. Similarly, the alternative interpolation yields $u_d = 171 \text{ m yr}^{-1}$, $u_b = 421 \text{ m yr}^{-1}$ and indicates that 71% of the observed surface velocity occurred as basal motion. Both of these estimates of u_d are considerably higher than that predicted by the shallow ice approximation of Glen's flow law, which suggests $u_d = 69 \text{ m yr}^{-1}$, and indicates that 88% of surface motion occurred at the bed (Figure 5c). Without further observations it is not possible to decompose basal motion into ice-sediment decoupling (e.g., Iverson et al., 1995) and deformation of the substrate itself.

4.4. Subglacial Water Electrical Conductivity

EC measurements recorded at the base of BH14c (M1; 603.3 m depth) and BH14d (M2; 615.9 m depth) were initially similar for the first 3 days, but then deviated with strikingly different patterns thereafter (Figure 7a). Following installation, the EC in BH14c and BH14d increased logarithmically to $10\text{--}15 \mu\text{S cm}^{-1}$ in less than 3 days (Figures 7a and 7c). For the shallower sensor, M1 in BH14c, the EC then continued to increase, attaining $35 \mu\text{S cm}^{-1}$ by the 17 August 2014, and then increased very rapidly to a peak of $81 \mu\text{S cm}^{-1}$ on 23 August (Figure 7a). The EC in BH14c then decreased to $\sim 2 \mu\text{S cm}^{-1}$ before the sensor failed on 18 October 2014. In contrast, the EC recorded by the deeper sensor, M2 in BH14d, varied consistently between 10 and $12 \mu\text{S cm}^{-1}$ until measurements ceased on 12 October 2014 (Figure 7a).

The 12 day long EC time series recorded by M3 at 619.2 m depth in BH16b is consistent with the measurements from 2014. EC in BH16b increased from low values (i.e., 2 to $4 \mu\text{S cm}^{-1}$) at an initially logarithmic and then relatively steady rate (Figure 7c). After 12 days the EC in BH16b attained $\sim 20 \mu\text{S cm}^{-1}$ (Figure 7b), similar to that recorded in BH14d after the same duration.

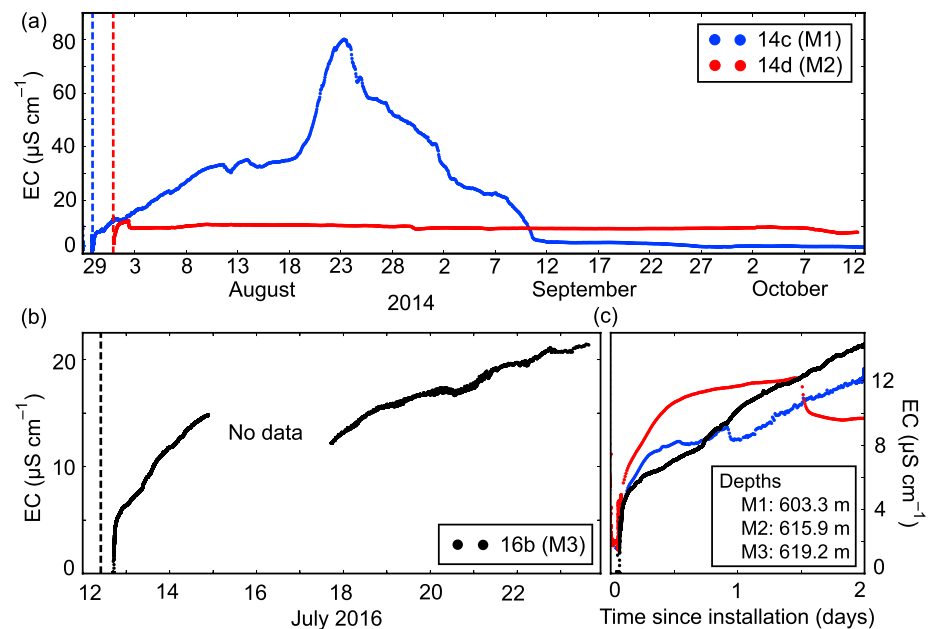


Figure 7. Time series of EC from (a) BH14c and BH14d, (b) BH16b, and (c) for the first 2 days after borehole breakthrough for all EC sensors. The color-coded vertical dashed lines on Figures 7a and 7b indicate the timing of borehole breakthrough events.

4.5. Turbidity

Turbidity measured at the base of BH16b at 619.2 ± 2 m depth in July 2016 was relatively constant and consistently below the linear calibration curve (Figure S7b). With a mean output voltage of 19 mV, the backscatter was lower than that in distilled water. Furthermore, the negligible variability (standard deviation of just 0.5 mV) can be entirely explained by the resolution of the data logger and electronic noise. We interpret this as evidence that the sensor was installed in optically thick sediment which almost completely prevented light transmission from the IR LED as we expect that even highly turbid water with a high SSC would give a higher, and more variable, backscatter than was observed.

4.6. Subglacial Water Pressure

In 2014, the deeper of the two pressure sensors, M2 in BH14d, failed first on 29 August 2014 presumably due to damage either to the cables or the sensors as it was dragged through or across the substrate. Although sensor M1 in BH14c operated considerably longer (until 21 October 2014), a notable increase in pressure was recorded on 10 September, coincident with M1 temperature falling below T_m (Figure S5), which we interpret as indicative of water expansion during the final phase of borehole freezing (cf. Engelhardt & Kamb, 1997; Ryser, 2014; Waddington & Clarke, 1995). The sensors therefore recorded subglacial water pressure for 28 and 42 days, respectively, through late summer and beyond the end of the 2014 melt season (Figure 8 and Table S2).

Postbreakthrough water levels in BH14c and BH14d stabilized at 79.2 m and 80.4 m below the ice surface, respectively (no firn was present; Table S1). These water levels would exert a pressure on the bed of 5.22 and 5.20 MPa, respectively. Using equation (9), and assuming reasonable values for the bulk density of ice ($\rho_i = 900 \pm 18 \text{ kg m}^{-3}$), gravitational acceleration ($g = 9.81 \pm 0.07 \text{ m s}^{-2}$ is), and the inclination angle ($\phi = 2.3 \pm 1^\circ$), an ice thickness h of 611 ± 5 m would exert an overburden pressure (p_i) of 5.39 ± 0.12 MPa. This is equivalent to a water level of 48.8 to 73.8 m below the surface. Hence, throughout the measurement period subglacial water pressure in BH14c and BH14d was high but never exceeded floatation, and remained 5.4 to 31.6 m below it. After applying an offset to correct for the different installation depths of the sensors, the pressure measurements from BH14c and BH14d are remarkably similar with only a slight discrepancy between the records, which increased through the period of contemporaneous data from 0.98 kPa on 2 August 2014 to 3.92 kPa on 29 August 2014 (Figure 8a).

Throughout our measurements in 2014 and 2016, subglacial water pressure was persistently high and varied between 5.11 and 5.21 MPa (Figure 8a), equating to an effective pressure ($N = p_i - p_w$) of 180 to 280 kPa

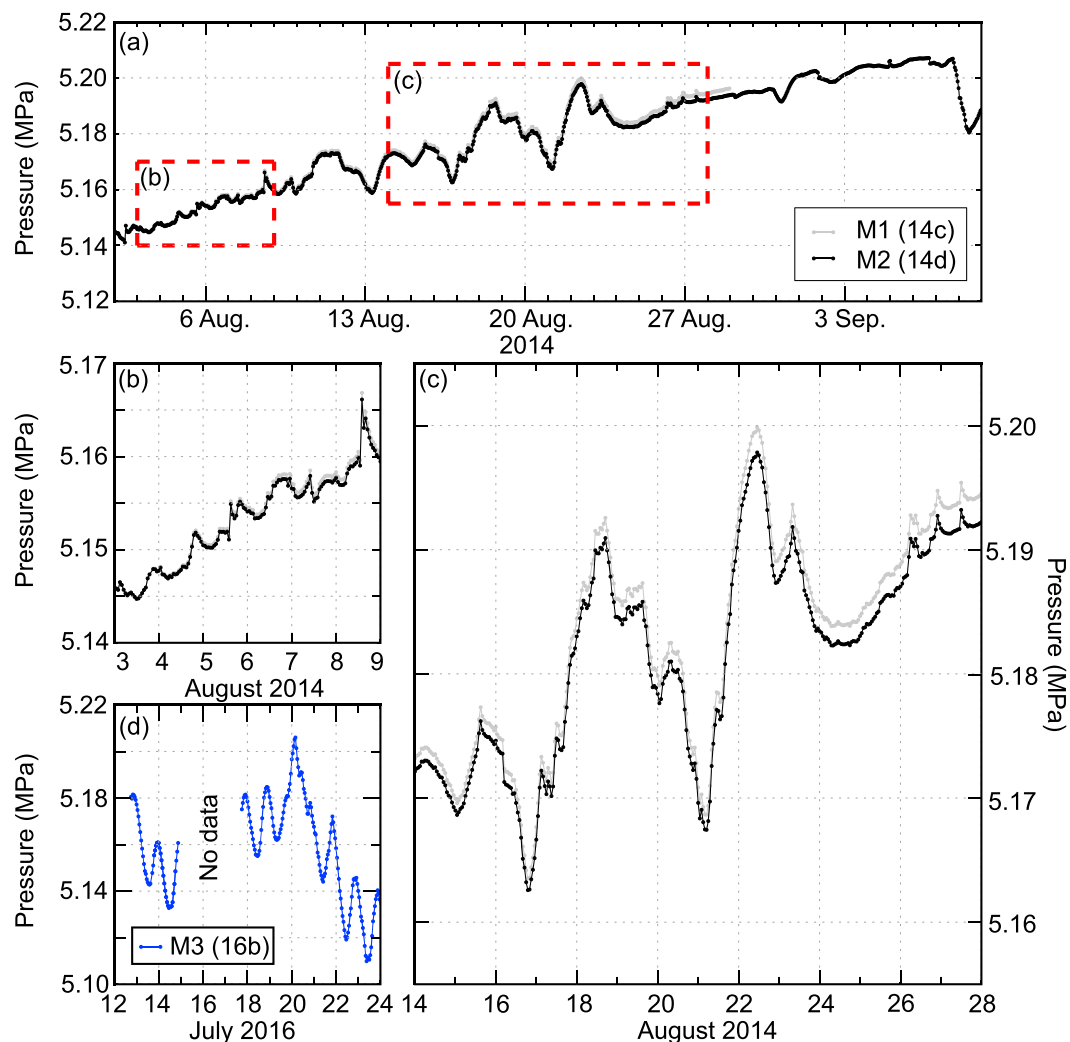


Figure 8. Pressure time series from (a–c) BH14c, BH14d and (d) BH16b. Figures 8b and 8c show enlarged sections of Figure 8a. Data are plotted at an hourly interval.

(Figures 9c and 9h). In 2014, short-term variations in subglacial water pressure, including diurnal fluctuations from 2 to 7 August, were superimposed upon a long-term linear increase of 1.77 kPa d^{-1} (Figures 8a and 8b). The diurnal variability in pressure was small with an amplitude of 4.9 kPa (Figure 8b). From 8–24 August 2014 these diurnal variations fade, though they never disappear completely, and the record becomes dominated by larger amplitude, multiday variations (Figure 8c).

Postbreakthrough, the water level recorded by sensor M3 in BH16b stabilized at 87.9 m below the surface (Table S1). From 12 to 24 July 2016, subglacial water pressure in BH16b exhibited a strong diurnal cycle with an amplitude of $\sim 29 \text{ kPa}$ (Figure 8d). A prominent peak in pressure on 20 July 2016, the highest recorded at 5.206 MPa , was coincident with a $\sim 30 \text{ h}$ period of heavy rainfall which halted drilling operations (Figure 9). After this rainfall event, subglacial water pressure decreased by $\sim 60 \text{ kPa}$ and the preceding diurnal cycle reestablished itself with the same amplitude.

4.7. Ice Motion

In 2014 discrete acceleration events were superimposed on a mean horizontal ice velocity of $\sim 590 \text{ m yr}^{-1}$. These acceleration events occurred on 9 August and 16–24 August and were associated with vertical displacements of 0.05 and 0.1 m , respectively (Figures 9e and 9j). During these events ice velocity increased by 7% and 17% , respectively, reaching maxima of 629 m yr^{-1} and 692 m yr^{-1} . In 2016 the mean ice velocity was higher at $\sim 650 \text{ m yr}^{-1}$ partly due to the earlier midsummer timing and partly because the GPS receiver was located $\sim 600 \text{ m}$ to the west on faster moving ice. Similar transient acceleration events also occurred in 2016

with velocities reaching maxima of $\sim 760 \text{ m yr}^{-1}$ and $\sim 1140 \text{ m yr}^{-1}$ on the 17 and 21 July, respectively. These accelerations were also associated with surface uplift events of 0.03 m and 0.1 m in magnitude. These discrete acceleration events are analyzed alongside the borehole sensor and meteorological time series in section 5.4.

5. Interpretation and Discussion

5.1. Nature of the Bed

Numerous lines of evidence indicate that the bed beneath S30 was soft sediment rather than hard bedrock. First, in all seven boreholes the drill's downward progress did not halt abruptly after breakthrough. In BH16c, for example, the drill continued below the breakthrough depth of 611.5 m at a slower, and more hesitant, rate with transient periods of partial unloading to 657 m depth where downward progress did cease completely (Figure S2; section 3.1). Second, no damage (e.g., dents or scratches) was sustained by the stainless steel drill stem, which often occurs when contact is made with hard bedrock (e.g., Harper et al., 2017). Strong support for the presence of sediment at the bed would have been the recovery of sediment on the drill stem: although this did not occur, it does not necessarily rule out the presence of sediment at the bed, as it could well have been washed off during the recovery of the drill stem through $\sim 520 \text{ m}$ of water to the surface. Finally, a 4 km long seismic profile acquired across S30 indicates a subglacial ice-sediment interface at $\sim 600 \text{ m}$ depth overlying a stratified sediment layer of up to $\sim 45 \text{ m}$ in thickness (Hofstede et al., 2018). Hence, we interpret the maximum borehole breakthrough depth (Figure 2 and Table S1) as indicative of an ice-sediment interface at $\sim 611 \text{ m}$ below the surface, with a sediment/bedrock interface below that at $\sim 657 \text{ m}$ depth. This interpretation suggests that M1 was installed within the lowermost section of an ice-walled borehole and that M2 and M3 were installed within a sediment layer (Figure 2). This assertion, which is based primarily on drilling records, is also consistent with (i) the observation that M1 at 603.3 m depth froze in after 42 d, (ii) the hesitant drilling below 611.5 m depth in BH16c, and (iii) the low and invariable backscatter measured by the turbidity sensor, M3, at 619.2 m depth in BH16b (Figure S7; section 4.5).

It is plausible that the overpressure in the boreholes ($\sim 500 \text{ kPa}$ at the base), which were initially water filled to the ice surface, may have initiated a hydraulic fracture which established a direct connection to the subglacial hydrological system (e.g., Iken et al., 1993). However, we prefer the simpler explanation that the drill directly intersected an ice-sediment interface and active subglacial hydrological system at $\sim 611 \text{ m}$ depth. If the boreholes did connect to the subglacial hydrological system via hydraulic fracture, our estimates of the ice-sediment interface at $\sim 611 \text{ m}$ depth would, by inference, be too shallow. Given the evidence described above, the ice-sediment interface is unlikely to be below the depths of M2 and M3 at 615.9 m and 619.2 m, respectively. Hence, we constrain the depth of the ice-sediment interface at between ~ 611 and $\sim 615 \text{ m}$, with the former considered more likely.

5.2. Thermal Regime

Englacial ice temperatures at S30 varied considerably with depth, from -21.25°C at 302 m below the surface to near-temperate conditions at the bed. The steeply curving temperature profile indicates that cold ice from higher elevations on the ice sheet is advected efficiently to site S30 due to the fast ice flow (e.g., Cuffey & Paterson, 2010). The temperature profile recorded at S30 is similar to that reported from $\sim 5 \text{ km}$ off the main flow unit of Jakobshavn Isbræ, where previous studies (Iken et al., 1993; Lüthi et al., 2002) reported minimum ice temperatures of -22.0°C located close to the center of the ice column at four sites ranging in thickness from 831 to $\sim 2,500 \text{ m}$. By comparison, ice temperatures on Sermeq Avannarleq (Lüthi et al., 2015) and Isunnguata Sermia (Harrington et al., 2015), two land-terminating glaciers in which the horizontal advection is lower due to slower (i.e., 100 to 150 m yr^{-1}) ice flow, were warmer, with minimum temperatures at sites of similar ice thickness to S30 ranging from -15°C to -6°C .

The temperature recorded by the lowest thermistor in BH14b, T1, persistently varied above T_m (Figure 4), and unless it malfunctioned (which we cannot exclude but do not expect, see section 4.2), it must have remained in liquid water or unfrozen sediment for the duration of its operation. The observation of basal temperatures that are 1.4°C above T_m contrast with the common assumption that subglacial water is close to thermal equilibrium with the surrounding ice. To our knowledge, such warm subglacial water temperatures (peaking at $+0.9^\circ\text{C}$) have only ever been reported once previously, from West Washmawapta Glacier in Canada (Dow et al., 2011). Dow et al. (2011) hypothesized that the warm water they measured could be emerging from a geothermally heated subglacial sediment aquifer, which would explain their observation of anticorrelation between water temperature and pressure—as warm groundwater emerged from the sediment at times of low subglacial

water pressure. Although T1 temperature did fall during a period of high subglacial water pressure from 10 to 14 August 2014, there is limited evidence for such an out of phase relationship in our data, and the T1 record remains enigmatic.

A kink in the S30 temperature profile was recorded by thermistor T8 at 302–451 m depth (or 49–73% of the ice thickness) with temperatures ~ 1 to 2°C warmer than would be predicted by interpolating the curve omitting T8 (Figure 5a). A similar kink in the temperature profile was observed by Lüthi et al. (2015) at their site GULL at 307–407 m depth (43–58% of the ice thickness). Such a kink could be explained by an englacial heat source such as surface-derived water refreezing in crevasses or moulins, but we cannot rule out the possibility that heat produced by englacial shearing could also play a role.

The linear trend in temperature for the lowest three thermistors at S30 (excluding T1 and M2) yield a temperature gradient ($\theta_b = dT/dZ$) just above the CTS of 0.03 K m^{-1} (Figure 6). The basal heat flux (Q) per unit area can hence be calculated at 60 mW m^{-2} :

$$Q = k_i \frac{dT}{dZ}. \quad (10)$$

The temperature gradient between T4 at 591.55 m depth and T6 at 501.94 m depth is larger still at 0.14 K m^{-1} , yielding a basal heat flux of 300 mW m^{-2} . Similar basal temperature gradients were calculated for Jakobshavn Isbræ: Iken et al. (1993) measured a temperature gradient in the lowermost $\sim 180\text{ m}$ of ice at their site A of 0.1 K m^{-1} , giving a basal heat flux of 210 mW m^{-2} . The geothermal heat flux has been estimated at $50\text{--}70\text{ mW m}^{-2}$ for this region using a variety of different approaches (Fox Maule et al., 2009; Pollack et al., 1993; Rogozhina et al., 2012, 2016; Shapiro & Ritzwoller, 2004) yet together with the frictional heat dissipation from enhanced basal motion, it does not adequately account for the elevated basal temperature gradient, since any temperate ice layer at the base would act as a barrier to upward heat conduction due to the Clausius-Clapeyron gradient (e.g., Funk et al., 1994). The strong basal heat flux is a product of the fast horizontal advection of cold ice from higher on the glacier and the energy provided near the bed by friction, ice deformation, geothermal heat, and the release of latent heat by water refreezing at the base.

Using our borehole and surface-based measurements we can calculate the average basal melt rate \dot{m} given a soft bed (Christoffersen & Tulaczyk, 2003):

$$\dot{m} = \frac{\frac{\partial T}{\partial Z} K_t - \theta_b k_i + \tau_b u_b}{\rho_i L_i}, \quad (11)$$

where \dot{m} is the basal melt rate, $\frac{\partial T}{\partial Z}$ is the vertical temperature gradient in the till, K_t is the thermal conductivity of till, θ_b is the basal ice temperature gradient (between T4 and T6), τ_b is the basal shear stress, and u_b is the basal velocity. The sediment heat flux ($\frac{\partial T}{\partial Z} K_t$) can be substituted with the reasonably well-constrained geothermal heat flux for this region of $50\text{--}70\text{ mW m}^{-2}$ (Fox Maule et al., 2009; Pollack et al., 1993; Rogozhina et al., 2012; Shapiro & Ritzwoller, 2004). The basal shear stress (τ_b) can be assumed to be equal to the shear strength (τ_f) of the subglacial sediment layer:

$$\tau_f = c + N \tan(\phi), \quad (12)$$

where c is the cohesion, $N = \rho_i - \rho_w$ is the effective normal stress, and ϕ is the sediment internal friction angle (Iverson et al., 1998). The cohesion can be assumed to be negligible for deforming till due to the low clay content (Cuffey & Paterson, 2010). To constrain N , we used the mean water pressure for the period of pressure measurements in 2014 (2–29 August 2014) and ice overburden pressure calculated using equation (9). The internal friction angle of the sediment does not vary much between sediments (Murray, 1997), and here we assume an angle of 30° , which is that of a Trapridge Glacier till (Clarke, 1987). The basal velocity u_b is constrained by that derived from the tilt measurements of $u_b = 373.0$ to 420.3 m yr^{-1} . Using these values and their ranges in equations (11) and (12) gives a mean basal melt rate \dot{m} of $13.6\text{--}15.4\text{ cm yr}^{-1}$. We note, however, that equation (11) does not account for any additional energy generated from the viscous heat dissipation of surface meltwater delivered to the ice-water interface (Mankoff & Tulaczyk, 2017), so the estimated basal melt rate is therefore likely to be a lower bound.

Our estimates of the ice-sediment interface at 611–615 m depth and the CTS at 607–615 m depth constrain temperate basal ice, if present, at no more than 8 m thick. Such a thin, or nonexistent, layer of temperate basal

ice at S30, which constitutes a maximum of 1.5% of the ice thickness, contrasts markedly with the limited number of temperature profiles reported from other outlet glaciers of the GrIS. For example, five temperature profiles on Isunnguata Sermia reported by Harrington et al. (2015) found temperate basal ice ranging in thickness from 20 to 100 m. Furthermore, Lüthi et al. (2002) provided a well-constrained estimate of a 31 m thick temperate basal layer (representing 3.7% of the ice thickness) at their site D on Jakobshavn Isbræ. This itself contrasts with the considerably thicker layer of temperate basal ice—of approximately several hundreds of meters—inferred for the ice stream's centerline by extrapolating and modeling a partial-depth temperature profile (Funk et al., 1994). The presence of a thick layer of temperate basal ice on the main flow unit of Jakobshavn Isbræ, which is thought to have been enlarged by enhanced vertical stretching (Iken et al., 1993; Funk et al., 1994), is supported by observations of basal ice in overturned icebergs discharged from the terminus (Lüthi et al., 2009). Importantly, on this basis these studies conclude that enhanced deformation within the thick temperate and pre-Holocene basal ice layers is a critical mechanism in the fast flow of Jakobshavn Isbræ (Funk et al., 1994; Iken et al., 1993; Lüthi et al., 2002, 2003).

The thin, or absent, layer of temperate basal ice observed at S30, in contrast to that apparent at Jakobshavn Isbræ, has several possible explanations. Faster basal motion has been shown to result in a thinner layer of temperate basal ice because basal melt driven by the frictional heat produced by basal motion results in a net downward flux of cold ice toward the CTS (Funk et al., 1994). Hence, the temperate basal ice could be thinner or absent at our site compared to the thicker layer observed at the drill sites on Jakobshavn because basal motion accounts for a larger proportion of overall ice flow at S30. This difference in the thickness of basal temperate ice between our drill site and the Jakobshavn Isbræ drill sites may, however, also be an artifact of the former being located near the centerline of Store, while the latter is located near the shear margin of Jakobshavn. A recent study by Shapero et al. (2016) indicates weak bed conditions beneath Jakobshavn centerline, which suggests high rates of basal motion (up to 70%) and high deformation rates at the lateral margin of the ice stream, which is where Lüthi et al. (2002) observed a 31 m thick layer of temperate basal ice. It is pertinent to note that such high rates of deformation relative to basal motion at lateral margins are a key characteristic of Antarctic ice streams, where they drive the formation of thick temperate ice layers at the margin, while temperate basal ice is absent on the centerline (Suckale et al., 2014; Perol & Rice, 2015). This suggests that extrapolation of a temperate basal ice layer observed at the lateral shear margin to the ice stream's centerline may not be valid. We note that the presence of a kink in the temperature profile at S30 would cause a partial depth profile to be misinterpreted: if, for example, our thermistor profile only extended from the surface to T8, extrapolating the temperature curve to the bed would overestimate temperatures within the lowermost 200 m of the ice column, and therefore overestimate the thickness of the basal temperate layer.

Notwithstanding these arguments, ice deformation accounted for 29–37% of surface motion at S30. While this confirms that ice deformation makes a significant contribution to the fast surface velocity, ice deformation cannot alone explain our observations which indicate that basal motion is the dominant component of Store Glacier's fast flow regime at this site.

5.3. Enhanced Ice Deformation in the Basal Zone

Analysis of the tilt measurements at S30 reveals enhanced deformation in the lowermost 50–100 m of the ice column (Figure 5b). Rates of deformation in the lowermost 100 m at S30 were approximately 5 times that recorded on Sermeq Avannarleq, where ice flow is 70–80 m yr⁻¹ (Ryser, Lüthi, Andrews, Hoffman, et al., 2014) but are slightly lower than those measured at site D on Jakobshavn Isbræ (Lüthi et al., 2003). By fitting a smooth interpolant to the horizontal velocity gradients we found that 61% of the internal deformation occurred in the lowermost 100 m of the ice column, with 29% in the lowermost 50 m. Previous borehole-based studies (e.g., Lüthi et al., 2002, 2003, 2015; Ryser, Lüthi, Andrews, Hoffman, et al., 2014) have attributed this basal zone of enhanced deformation to a layer of pre-Holocene ice deposited in the last glacial period (i.e., the Wisconsin). These studies, together with radio echo sounding surveys (Karlsson et al., 2013), estimated the HWT in West Greenland at relative depths ranging from 82 to 85% of the ice thickness. Strong englacial reflections were observed in the seismic data at the drill site at 528–566 m depth (Hofstede et al., 2018), and the upper surface of this reflector is at a depth of 86% of the ice thickness. Furthermore, the ice layer from which these englacial seismic reflections originate is similar in thickness and depth to a layer of lower electrically conductive ice at site FOXX of Ryser, Lüthi, Andrews, Hoffman, et al. (2014), which was interpreted as representing the HWT. Hence, we infer that the HWT at S30 is at a depth of 528 m below the surface. Consistent with previous observations, there is no evidence for a step or kink in the temperature profile at the HWT, but the observation of enhanced deformation (Figure 5) in the Wisconsin ice (Paterson, 1991) would explain the

steep basal temperature gradient (Figure 5a) and the necessary change in crystal orientation fabric required to explain the seismic reflections (Horgan et al., 2008). Following previous studies (Lüthi et al., 2002; Ryser, Lüthi, Andrews, Hoffman, et al., 2014), if we assume that deformation rates increase sharply at the HWT (i.e., by invoking the alternative interpolant on Figure 5) we find that 69% of the internal deformation occurred in the lowermost 100 m of the ice column, with 63% of deformation below the HWT.

The lowermost tilt sensor A1 at 601.2 m depth recorded the lowest rate of deformation of 0.106 yr^{-1} , which is 12 times lower than expected from theory and markedly different from that recorded by adjacent sensor A3 at 592 m depth. A1 was installed 0.3 m above thermistor T1, which never froze in, and the low deformation rate at A1 could therefore be explained by poor coupling to the ice due to unfrozen or temperate conditions. On the other hand, the relatively steady tilt time series (Figure S4) suggests that the sensor was coupled to the ice, and it is therefore possible that our measurements highlight heterogeneous deformation rates near the bed. This assertion is supported by previous studies where a greater number of sensors reveal deformation rates varying considerably with depth, particularly below the HWT (Lüthi et al., 2003; Ryser, Lüthi, Andrews, Hoffman, et al., 2014). Such heterogeneity in ice deformation rates near the bed have been explained by horizontal stress transfer from slippery to sticky patches (e.g., Ryser, Lüthi, Andrews, Catania, et al., 2014), impurity content, and variable ice crystallography (e.g., Lüthi et al., 2002).

With the exception of the deepest sensor (A1), the horizontal velocity gradients derived from our borehole tilt measurements are considerably greater than that predicted by theory (Table 1; Figure 5b). Deformation rates at sensors A3, A4, and A5 were 1.5, 4.0, and 7.0 times greater than theoretical estimates (Table 1 and Figure 5b). The poor match between theory and measurements at S30 is, however, unsurprising given the enhanced rates of basal motion at this site, and the disregard of longitudinal (higher-order) stress gradients in calculating englacial deformation under Glen's flow law.

Enhanced shear strain within the lowermost 50–100 m of the ice column is further supported by the dates that individual sensors stopped working—interpreted as resulting from their cables snapping. Thermistors below ~550 m depth stopped working after 76–93 days, while thermistors above ~500 m depth continued to operate correctly for at least 343 days (Table S2), with the exception of (typically negative) jumps in recorded temperature consistent with episodic cable strain. Hence, we can constrain a transition to enhanced deformation rates at 500–550 m below the surface, which is consistent with the deformation profile (Figure 5b), and a strong englacial seismic reflector at ~528 m depth (Hofstede et al., 2018), which we infer represents the transition to more deformable pre-Holocene ice.

5.4. Temporal Variability

To assess the principal drivers of ice flow variability at S30, contemporaneous time series of near-surface air temperature, reanalysis precipitation rate, surface ablation, subglacial water pressure and EC, and surface velocity and uplift are presented (Figure 9). In particular, distinct episodes of sustained high ice velocity that occurred on 16–24 August 2014, 17 July 2016, and 20–21 July 2016 are analyzed.

From 16 to 18 August 2014 surface velocity increased by 17% from $\sim 590 \text{ m yr}^{-1}$ to 692 m yr^{-1} accompanied by 0.1 m of vertical surface uplift (Figure 9e). The ensuing period of enhanced flow was broad and asymmetric: characterized by a rapid rise and a slow decay in ice velocity over an 8–9 d period. The episode consisted of two distinct velocity maxima on 18 and 21 August that were preceded by peak surface ablation rates of 55 and 56 mm d^{-1} on the 17 and 20 August, respectively (Figures 9a and 9e). Near-surface air temperatures were continuously above freezing throughout the day and night (Figure 9a) indicating that the elevated daily ablation totals were associated with the advection of a warm air mass over this site, coupled with a reduction in nighttime cooling due to the longwave cloud effect (e.g., Doyle et al., 2015; Van Tricht et al., 2016). This assertion is supported by the passage of a low-pressure system (minimum of 991 hPa) over Baffin Bay during this period (Movie S9). Peaks in the reanalysis precipitation rate of 22.3 mm d^{-1} , 19.3 mm d^{-1} , and 22.7 mm d^{-1} on the 16, 17, and 20 August coincided with peaks in relative humidity of >95%, indicating that rainfall contributed to surface runoff (rainfall plus melt minus refreezing) at this time (Figures 9b and 9g). Although the magnitude of the surface height peaks during this time period were small with an amplitude of <0.1 m, there is evidence that peaks in surface velocity were coincident with peaks in uplift rate rather than absolute surface height, which is indicative of cavity opening through hydraulic-ice bed separation (e.g., Iken et al., 1983). On 21 August the ice surface was vertically raised $\sim 0.08 \text{ m}$ above its preceding level (Figure 9e), and the gradual decline of surface height which followed can be interpreted as the slow release of stored water at the bed (e.g., Iken et al., 1983). The relationship between subglacial water pressure and ice motion is more

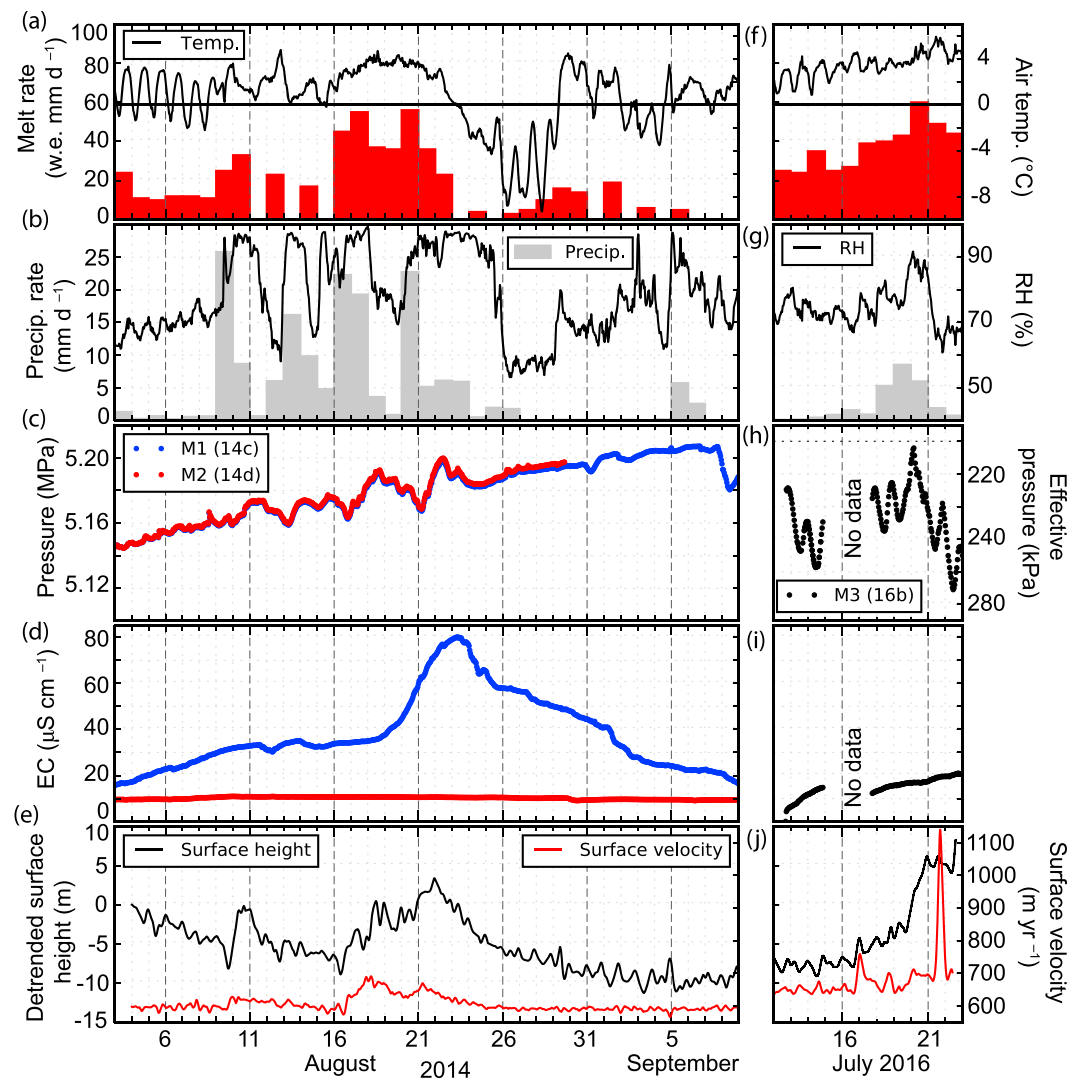


Figure 9. Time series of (a) near-surface air temperature and melt rate, (b) precipitation rate and relative humidity, (c) subglacial water pressure and effective pressure, (d) EC, and (e) horizontal surface velocity and linearly detrended surface height in 2014. (f–j) Same as Figures 9a to 9e but for 2016.

difficult to determine. Although peaks in subglacial water pressure occurred during this event, they do not consistently lead or lag either surface uplift or ice velocity (Figure 9). There is therefore no evidence of a direct anticorrelation between subglacial water pressure and ice velocity as some previous studies have observed (Andrews et al., 2014; Murray & Clarke, 1995). Finally, during this event, the tilt sensors (see supporting information S1, section 3.6) registered anomalously high changes in acceleration and tilt (Figure S4). These acceleration events may be similar to those recorded by Lüthi et al. (2003) on Jakobshavn Isbræ where they are attributed to some combination of enhanced basal motion, internal deformation, and brittle fracture.

A prominent peak in the EC recorded by the shallower basal sensor, M1 in BH14c, of up to $81 \mu\text{S cm}^{-1}$ on 23 August 2014 may also be associated with high magnitude runoff during this rainfall/melt event (Figure 9d). The interpretation of this EC peak is, however, complicated by the observation that the water temperature measured by thermistor M1 (mounted adjacent to the EC sensor) during this period was in thermal arrest prior to freezing on ~8–10 September (Figure S5). This EC spike could therefore be at least partly explained by the concentration of solutes associated with the progressive closure of the borehole during freezing. The observed thermal arrest indicates that at this time the EC sensor would have been enclosed in an ice-water mixture, and the temperature gradient (Figure 6) indicates that the borehole froze from the top downward. It is therefore plausible that M1 detected the disturbance of subglacial sediments as a high concentration of

solutes within the subglacial hydraulic system due to an abrupt increase in water flux following the rainfall/melt event (e.g., Bartholomew et al., 2011; Gordon et al., 1998). If this interpretation is correct, then the persistently low and invariable contemporaneous EC recorded by M2 installed at 615.3 m, 12.6 m lower than M1, can be explained by the installation of M2 within the sediment layer. This would be entirely consistent with the interpretation of an ice-sediment interface at 611 m depth (see section 5.1) and is further supported by the relatively steady EC recorded at 619.1 m depth in BH16b, which did not vary in response to similar runoff events (Figure 9). From these interpretations, we infer that at least during high-magnitude runoff events subglacial water flow preferentially occurs at the ice-sediment interface, with an additional component of Darcian flow within the sediment layer.

An additional ice flow acceleration event occurred on 17 July 2016, but unfortunately there are no pressure or EC records to complement it (Figure 9). The surface velocity peak of 760 m yr^{-1} was, however, coincident with a transient vertical displacement of 0.03 m and a 45% increase in the ablation rate from 27 mm we d^{-1} on 16 July to 39 mm we d^{-1} on 17 July (Figure 9f). A further exceptional ice flow event on 20–21 July represents the highest recorded instantaneous velocity of $1,140 \text{ m yr}^{-1}$ at 16:50 on 21 July 2016 and the highest recorded subglacial water pressure in 2016 of 5.21 MPa at 03:20 on 20 July. During this event, the peak water pressure was superimposed on a strong diurnal cycle and was coincident with both heavy rainfall, totalling 21.7 mm from 18 to 21 July, and high melt rates, which peaked at 61 mm we d^{-1} on 20 July 2016 (Figure 9). The maximum recorded velocity occurred at the end of a 3 day period of sustained uplift of 0.1 m relative to the preceding level and lagged behind peak ablation and peak rainfall by 2 and 3 days, respectively. Both of the July 2016 events described above were associated with the passage of low-pressure systems that tracked over Baffin Bay advecting warm moist air over S30 (Figure S10).

The diurnal variability in subglacial water pressure (Figures 8b and 8d) and covariations in surface velocity and uplift described above (Figure 9) confirm that surface runoff directly accessed the bed and modulated rates of basal motion at S30 (e.g., Iken et al., 1983). The greater amplitude of the diurnal pressure variations in mid-July 2016 (Figure 8d) is most likely due to their earlier, midsummer timing compared to the 2014 borehole measurements, which commenced close to the end of the melt season. The seasonal timing may also partly explain the higher background ice velocity recorded in 2016 compared to 2014 (Figures 9e and 9j), although some of this disparity can be explained by the GPS receiver in 2016 being located $\sim 600 \text{ m}$ to the west of the 2014 receiver and drill site, where mean annual ice velocity was higher. Taking the two highest velocities recorded in 2016 as an example, the peaks in velocity of 760 and $1,140 \text{ m yr}^{-1}$ on 17 and 21 July 2016 represent increases in velocity of 6% and 81% above average, respectively. This indicates that ice flow at S30 is proportionally less sensitive to surface melt inputs than ice flow along the slow-flowing land-terminating margin where ice velocities typically increase by more than 100% above the long-term mean in the summer (e.g., Bartholomew et al., 2010). This is in accordance with satellite feature tracking of ice sheet flow across West Greenland (Joughin, Das, et al., 2008) and could be further explained at S30 by a mechanism of rapid basal motion facilitated by a soft bed experiencing persistently high subglacial water pressure, as modelled by Bougamont et al. (2014). Nevertheless, small (i.e., $< 0.5\%$ of overburden) variations in subglacial water pressure were coincident with relatively large (e.g., 6–81%) variations in surface velocity (Figure 9). Furthermore, in contrast to observations from other glaciers and regions of the GrIS (e.g., Doyle et al., 2015; Meier et al., 1994) there was no evidence in our data sets for subsequent “extra slowdowns” following such high-velocity events. Hence, the degree to which basal motion is modulated by surface water inputs and the evolution of the subglacial drainage system at fast-flowing, marine-terminating glaciers appears to be limited at the timescale of our analysis and remains unevaluated in the longer term.

5.5. Subglacial Hydrology

The measurement of consistently high subglacial water pressure of 5.11 to 5.21 MPa (equivalent to 94.8 to 96.7% of the ice overburden pressure) with low-amplitude variability (up to $\sim 29 \text{ kPa}$, equivalent to 0.5% of the ice overburden pressure) indicates a subglacial hydrological system operating at sustained high pressure. Existing theory suggests that such high subglacial water pressures, which are a necessary precondition for fast basal motion, are sustained at the bed because the development of efficient, low-pressure drainage systems (e.g., R channels; Röthlisberger, 1972) is hindered by the rapid closure of conduits due to fast ice motion, and sediment infill if present (e.g., Kamb, 1987). Our measurements indicate that effective pressure ranged between 180 and 280 kPa (Figures 9c and 9h), which is below the theoretical threshold of 400–500 kPa proposed by Kamb et al. (1994) to approximate the transition between “normal” glacier flow at effective pressures above the threshold and “continuous surging” at values below it. Similar measurements made at site A on

Jakobshavn Isbræ by Iken et al. (1993), indicate an effective pressure of approximately 380 kPa. Both of these measurements markedly contrast with observations of lower subglacial water pressure (down to 70% of overburden) with greater variability (e.g., ~17% of overburden) measured in moulins on the GrIS (Andrews et al., 2014; Cowton et al., 2013), which are broadly consistent with measurements from the limited number of boreholes on temperate alpine glaciers that are believed to have directly intersected major subglacial channels (Fountain, 1994; Hubbard et al., 1995). This disparity corroborates that the boreholes drilled to the bed at S30 did not intersect an efficient component of the subglacial drainage system. Our observations also contrast with all other measurements from slow-flowing regions of the GrIS, which are typically characterized by greater variability in subglacial water pressure (i.e., within the range of 2–10% of overburden), with the largest variability recorded near land-terminating margins (e.g., Andrews et al., 2014; Meierbachtol et al., 2013; van de Wal et al., 2015; Wright et al., 2016).

The observations at S30 of rapid borehole drainage during breakthrough with coincident spikes in subglacial water pressure, EC, and temperature measured in adjacent boreholes (Figures 3, 4, S3, and Movie S8), does however suggest that the boreholes were connected at the bed by an active subglacial hydrological system. All seven boreholes drained rapidly at depths of 605.3–611.5 m below the ice surface. Similar observations of rapid borehole drainage have been made at several sites on Jakobshavn Isbræ in Greenland (Iken et al., 1993; Lüthi et al., 2002), Trapridge (Stone & Clarke, 1996); Columbia (Meier et al., 1994); and Variegated glaciers in Alaska (the latter only while in surge; Kamb & Engelhardt, 1987), Glacier Perito Moreno in Argentinian Patagonia (Sugiyama et al., 2011), and Ice Stream B in Antarctica (Engelhardt & Kamb, 1997). Although rapid borehole drainage has been observed infrequently on temperate valley glaciers including Haut Glacier d'Arolla (Gordon et al., 2001; Hubbard et al., 1995), Blue Glacier (Engelhardt, 1978), and polythermal Gornergletscher (Iken et al., 1996), it appears to be a feature that is more common on fast-flowing ice masses than on ice that is flowing more slowly. Examples of the latter (i.e., boreholes draining slowly or not at all) include boreholes drilled at site FOXX on Sermeq Avannarleq (Andrews et al., 2014) and Isunnguata Sermia (Meierbachtol et al., 2016) in West Greenland, Small River Glacier in British Columbia (Smart, 1996), and interstream ice ridges adjacent to Ice Stream B in Antarctica (Engelhardt & Kamb, 1997). Hence, although a strict rule may not exist, the frequency of rapid and immediate borehole drainage could provide an insight into the contrasting nature of the subglacial hydrological systems beneath fast- and slow-flowing ice masses.

Previous studies (e.g., Andrews et al., 2014; Gordon et al., 2001; Hoffman et al., 2016) interpreted boreholes that drained either slowly or not at all as connected to a region of the bed isolated from the subglacial hydrological system. Such isolated boreholes are often characterized by anticorrelated variations in subglacial water pressure and surface velocity (e.g., Andrews et al., 2014) due to the mechanical transfer of load from hydraulically connected areas (Murray & Clarke, 1995; Ryser, Lüthi, Andrews, Catania, et al., 2014). Our measurements of surface velocity and subglacial water pressure (see section 5.4) contrast with this, confirming that our boreholes connected with an active subglacial hydrological system. Furthermore, Meier et al. (1994) interpreted the apparent ease at which boreholes connected with the subglacial drainage system on surging glaciers as evidence for a more pervasive development of the subglacial drainage system and basal fractures, thought to be broadly consistent with the linked-cavity theory of subglacial drainage (Kamb, 1987). Accordingly, it is pertinent that our observations of (i) rapid borehole drainage, (ii) persistently high subglacial water pressure with low-amplitude variability, and (iii) EC were similar across all boreholes drilled over 2 years (Figures 7–9). Hence, within the spatial and temporal limits defined by the borehole spacing and timing (i.e., within a 10 m² area in 2014; and 50 m to the northeast in 2016; Figure 1c), these observations suggest that the active subglacial hydrological system beneath S30 was spatially and temporally homogenous.

Rapid borehole drainage and pressure impulses during breakthrough in neighboring boreholes have previously been interpreted as either resulting from drainage through permeable sediments, or through a gap separating the ice from the substrate (Engelhardt & Kamb, 1997; Lüthi, 1999; Stone & Clarke, 1993). Assuming a borehole with a uniform diameter of 0.15 m, the large (~80 m) and rapid (~120 s) drop in water levels in BH14c and BH14d indicates that the subglacial drainage system had the capacity to accommodate an estimated 1.4 m³ of water in this time. It is plausible that this volume of water was initially accommodated in a cavity created by localized ice bed separation which then drained slowly either through sediments or a narrow conduit (Engelhardt & Kamb, 1997; Lüthi, 1999). The rapid pressurization of the subglacial drainage system observed in BH14c following the drainage of BH14d and the slow recovery to preceding levels over ~15 h, is consistent with similar observations of interborehole, asymmetric pressure impulses on Jakobshavn Isbræ (Lüthi, 1999) and Ice Stream B in Antarctica (Engelhardt & Kamb, 1997). We interpret the slow recovery of

water pressure (Figure S3a) as indicative of low hydraulic transmissivity within the subglacial drainage system. Unfortunately, the close spacing of our boreholes relative to their positioning accuracy is too short to calculate sediment transmissivity in the manner described in Lüthi (1999). The hypothesis of drainage through a sediment layer with low hydraulic transmissivity is, however, supported by the initially logarithmic post-drilling rate of EC increase (Figure 7c), which we take to indicate that the low EC (i.e., 1 to $2 \mu\text{S cm}^{-1}$) surface water delivered to the bed during drilling diluted the relatively high background EC of the subglacial water (i.e., 10 – $20 \mu\text{S cm}^{-1}$), and that this dilution was not recovered immediately due to the slow influent percolation of relatively high EC water from the surrounding area. The logarithmic recovery of background EC after drilling, which took over 12 h before the rate of increase abated, was consistent across all three boreholes sampled (BH14c, BH14d, and BH16b), drilled in two different years (Figure 7c). Together, these observations can be interpreted as indicative of drainage at the ice-sediment interface during borehole breakthrough and Darcian flow through a permeable, subglacial sediment layer thereafter. Furthermore, the decrease in the drainage time with each consecutive borehole breakthrough (Figure 3) suggests that the perturbation of the subglacial environment by the injection of drilling water and heat into the subglacial environment may have increased the transmissivity of the subglacial hydrological system in the vicinity of the borehole's base.

The underlying linear increase in subglacial water pressure measured in BH14c and BH14d in August 2014 (Figure 8a) is consistent with several borehole studies that document the seasonal transition from summer into winter (Andrews et al., 2014; Fountain, 1994; Hubbard & Nienow, 1997; Lüthi et al., 2002; Wright et al., 2016). Lüthi et al. (2002) attributed a similar gradual late-summer increase in subglacial water pressure of 1.47 kPa d^{-1} on Jakobshavn Isbræ to an increase in the ice thickness. At S30 the observed linear increase in subglacial water pressure in BH14c of 1.77 kPa d^{-1} between 2 August and 7 September 2014 would be equivalent to an ice thickening rate of 0.2 m d^{-1} and a vertical strain rate of 0.1 yr^{-1} . Although such high rates of vertical strain are plausible, this apparently systematic pattern could also be explained by the progressive closure of the subglacial hydrological system, and the boreholes connection to it, as surface melt inputs decline (e.g., Doyle et al., 2015; Fountain, 1994).

Crevasses in the immediate vicinity of the S30 drill site were continuously water filled. However, active supraglacial drainage into moulins and crevasses did occur $\sim 700 \text{ m}$ to the west. It is therefore possible that such drainage has the capacity to form efficient subglacial drainage pathways in our study area and that such spatially discrete subglacial hydrological systems were not sampled by the boreholes we drilled. The relatively small surface catchment size, due to the high density of crevasses on Store Glacier compared to slower regions of the ice sheet, suggests that the delivery of surface water to the bed generally involves much smaller water fluxes distributed over a larger area, which has important implications for the development of efficient subglacial hydrological systems (Banwell et al., 2016; Colgan et al., 2011). We note that the diurnal pressure variations we observed (Figures 8b and 8d) are likely to originate from diurnally varying surface melt inputs into the surrounding moulins and crevasses, which theory and observations suggest is likely to flow in an efficient, channelized hydrological system (e.g., Andrews et al., 2014; Röthlisberger, 1972). The lack of accompanying diurnal EC and turbidity variations (Figures 7 and S7) suggests, however, that only the variations in water pressure were effectively transmitted to our boreholes. We infer that this occurs via inefficient drainage through or above a subglacial sediment layer (cf. Hubbard et al., 1995), although an alternative hypothesis that longitudinal or shear stress variations transmitted through the ice can drive variations in the normal stress and therefore water pressure is also plausible (Ryser, Lüthi, Andrews, Catania, et al., 2014). Hence, although our borehole data sets are inconsistent with the interception of an efficient subglacial channel we cannot rule out the existence of such channels in the vicinity.

Overall, our measurements of the subglacial hydrological system are similar to those from fast-flowing marine-terminating glaciers (Lüthi et al., 2002; Meier et al., 1994), ice streams (e.g., Engelhardt & Kamb, 1997), and glaciers in surge (Kamb et al., 1985) and we interpret this as evidence of broadly similar physical and hydraulic conditions beneath these ice masses. Specifically, we argue that the fast basal motion of these ice masses, and of Store Glacier, is enabled by deformable subglacial sediments and ice-sediment decoupling (Iverson et al., 1995) together with persistently high subglacial water pressures maintained by—and in turn facilitating—fast, basal motion. Based on our interpretation of all the borehole measurements presented herein, we hypothesize that the hydrological regime beneath S30 consists of inefficient water flow through, and possibly above, a thick subglacial sediment layer (e.g., Creyts & Schoof, 2009; Walder & Fowler, 1994).

6. Conclusions

Borehole-based measurements of (i) englacial temperature and tilt; and (ii) subglacial water pressure, EC, and turbidity were obtained during the summers of 2014 and 2016 from a site located 30 km from the terminus of Store Glacier. Together with surface meteorological and GPS measurements, these data sets provide insights into the thermal structure, flow regime, and the physical conditions within and beneath Store Glacier at this location.

Our measurements reveal a steeply curving temperature profile characteristic of fast ice flow, and the presence of a thin (i.e., 0–8 m) layer of basal temperate ice. With a sliding ratio of 60–70% we find that ice flow at this site was dominated by basal motion. Internal deformation accounts for the remaining 30–40% of the mean annual flow rate of $\sim 600 \text{ m yr}^{-1}$ and was concentrated in the lowermost $\sim 100 \text{ m}$ of the ice column, which potentially includes $\sim 80 \text{ m}$ of more deformable pre-Holocene ice. Effective pressures were low (180 to 280 kPa) due to persistently high subglacial water pressures which we interpret as indicative of water flow through an inefficient subglacial hydrological system. From detailed analysis of our records, we hypothesize that the subglacial drainage system comprises water flow at the ice-sediment interface and within the subglacial sediment layer. Small variations in subglacial water pressure were coincident with relatively large variations in ice surface velocity and uplift, indicating that basal motion at this site is sensitive to inputs of melt and meteoric water from the surface. We infer that the fast basal motion at S30 is facilitated by low effective pressures and some combination of deformable subglacial sediments and ice/sediment decoupling.

Our observations are consistent with similar measurements reported from fast-flowing, soft-bedded ice masses such as marine-terminating glaciers in Alaska, ice streams in Antarctica and glaciers in surge, and we hypothesize that several key properties are common to all of these ice masses.

Acknowledgments

This research was funded by UK National Environment Research Council grants NE/K006126 and NE/K005871/1 and an Aberystwyth University Capital Equipment grant to B. H. A. H. gratefully acknowledges support from the BBC's Operation Iceberg program for the deployment of the GPS reference station and a Professorial Fellowship from the Centre for Arctic Gas Hydrate, Environment and Climate, funded by the Research Council of Norway through its Centres of Excellence (grant 223259). The authors thank the crew of *SV Gambo* for logistical support, Ann Andreasen and the Uummannaq Polar Institute for hospitality, technicians Barry Thomas and Dave Kelly for assembly of the borehole sensors, Joe Todd for producing a bed elevation model from mass conservation that proved useful in selecting the drill site, and Leo Nathan for assistance in the field. NCEP/NCAR Reanalysis data were provided by the NOAA/OAR/ESRL PSD, Boulder, Colorado, USA, from www.esrl.noaa.gov/psd/. The data sets presented in this paper are available for download from <https://doi.org/10.6084/m9.figshare.5745294>.

References

- Ahn, Y., & Box, J. (2010). Glacier velocities from time-lapse photos: Technique development and first results from the Extreme Ice Survey (EIS) in Greenland. *Journal of Glaciology*, *56*(198), 723–733.
- Andrews, L. C., Catania, G. A., Hoffman, M. J., Gulley, J. D., Luthi, M. P., Ryser, C., ... Neumann, T. A. (2014). Direct observations of evolving subglacial drainage beneath the Greenland Ice Sheet. *Nature*, *514*(7520), 80–83. <https://doi.org/10.1038/nature13796>
- Banwell, A., Hewitt, I., Willis, I., & Arnold, N. (2016). Moulin density controls drainage development beneath the Greenland Ice Sheet. *Journal of Geophysical Research: Earth Surface*, *121*, 2248–2269. <https://doi.org/10.1002/2015JF003801>
- Bartholomew, T., Anderson, R., & Anderson, S. P. (2011). Growth and collapse of the distributed subglacial hydrologic system of Kennicott Glacier, Alaska, USA, and its effects on basal motion. *Journal of Glaciology*, *57*(206), 985–1002. <https://doi.org/10.3189/002214311798843269>
- Bartholomew, I., Nienow, P., Mair, D., Hubbard, A., King, M., & Sole, A. (2010). Seasonal evolution of subglacial drainage and acceleration in a Greenland outlet glacier. *Nature Geoscience*, *3*, 408–411. <https://doi.org/10.1038/ngeo863>
- Bartholomew, I., Nienow, P., Sole, A., Mair, D., Cowton, T., Palmer, S., & Wadham, J. (2011). Supraglacial forcing of subglacial drainage in the ablation zone of the Greenland ice sheet. *Geophysical Research Letters*, *38*, L08502. <https://doi.org/10.1029/2011GL047063>
- Bayley, O. (2007). Temperature of a “temperate” alpine glacier: Glacier De Tsanfleuron, Switzerland (PhD thesis). UK: Aberystwyth University, Wales.
- Bougamont, P., Christoffersen, M., Hubbard, A., Fitzpatrick, A., Doyle, S., & Carter, S. (2014). Sensitive response of the Greenland Ice Sheet to surface melt drainage over a soft bed. *Nature Communications*, *5*, 5052. <https://doi.org/10.1038/ncomms6052>
- Brennan, P. V., Lok, L. B., Nicholls, K., & Corr, H. (2014). Phase-sensitive FMCW radar system for high-precision Antarctic ice shelf profile monitoring. *IET Radar, Sonar & Navigation*, *8*(7), 776–786. <https://doi.org/10.1049/iet-rsn.2013.0053>
- Chauché, N., Hubbard, A., Gascard, J.-C., Box, J. E., Bates, R., Koppes, M., ... Patton, H. (2014). Ice-ocean interaction and calving front morphology at two west Greenland tidewater outlet glaciers. *The Cryosphere*, *8*(4), 1457–1468. <https://doi.org/10.5194/tc-8-1457-2014>
- Chen, G. (1998). GPS kinematic positioning for the airborne laser altimetry at Long Valley, California (PhD thesis). Cambridge: Massachusetts Institute of Technology.
- Christoffersen, P., & Tulaczyk, S. (2003). Response of subglacial sediments to basal freeze-on: 1. Theory and comparison to observations from beneath the West Antarctic ice sheet. *Journal of Geophysical Research*, *108*(B4), 2222. <https://doi.org/10.1029/2002JB001935>
- Clarke, G. K. C. (1987). Subglacial till: A physical framework for its properties and processes. *Journal of Geophysical Research*, *92*(B9), 9023–9036. <https://doi.org/10.1029/JB092iB09p09023>
- Colgan, W., Steffen, K., McLamb, W., Abdalati, W., Rajaram, H., Motyka, R., ... Anderson, R. (2011). An increase in crevasse extent, West Greenland: Hydrologic implications. *Geophysical Research Letters*, *38*, L18502. <https://doi.org/10.1029/2011GL048491>
- Cowton, T., Nienow, P., Sole, A., Wadham, J., Lis, G., Bartholomew, I., ... Chandler, D. (2013). Evolution of drainage system morphology at a land-terminating Greenlandic outlet glacier. *Journal of Geophysical Research: Earth Surface*, *118*, 29–41. <https://doi.org/10.1029/2012JF002540>
- Creys, T. T., & Schoof, C. G. (2009). Drainage through subglacial water sheets. *Journal of Geophysical Research*, *114*, F04008. <https://doi.org/10.1029/2008JF001215>
- Csatho, B. M., Schenk, A. F., van der Veen, C. J., Babonis, G., Duncan, K., Rezvanbehbahani, S., ... van Angelen, J. H. (2014). Laser altimetry reveals complex pattern of Greenland Ice Sheet dynamics. *Proceedings of the National Academy of Sciences of the United States of America*, *111*(52), 18,478–18,483. <https://doi.org/10.1073/pnas.1411680112>
- Cuffey, K., & Paterson, W. (2010). *The Physics of Glaciers* (4th ed.). Burlington: Elsevier.
- Dow, C., Kavanaugh, J., Sanders, J., Cuffey, K., & MacGregor, K. (2011). Subsurface hydrology of an overdeepened cirque glacier. *Journal of Glaciology*, *57*(206), 1067–1078. <https://doi.org/10.3189/002214311798843412>

- Dow, J., Neilan, R. E., & Rizos, C. (2009). The International GNSS Service in a changing landscape of Global Navigation Satellite Systems. *Journal of Geodesy*, 83, 191–198. <https://doi.org/10.1007/s00190-008-0300-3>
- Doyle, S., Hubbard, A., van de Wal, R., Box, J., van As, D., Scharer, K., ... Hubbard, B. (2015). Amplified melt and flow of the Greenland ice sheet driven by late-summer cyclonic rainfall. *Nature Geoscience*, 8(8), 647–653. <https://doi.org/10.1038/ngeo2482>
- Engelhardt, H. (1978). Water in glaciers: Observations and theory of the behaviour of water levels in boreholes. *Z Gletschkd Glazialgeol*, 14, 35–60.
- Engelhardt, H., & Kamb, B. (1997). Basal hydraulic system of a West Antarctic ice stream: Constraints from borehole observations. *Journal of Glaciology*, 43(144), 207–229. <https://doi.org/10.3198/1997JoG43-144-207-230>
- Engelhardt, H., Humphrey, N., Kamb, B., & Fahnestock, M. (1990). Physical conditions at the base of a fast moving Antarctic ice stream. *Science*, 248(4951), 57–59. <https://doi.org/10.1126/science.248.4951.57>
- Fenn, C. (1987). *Glacio-fluvial sediment transfer: An alpine perspective, chap. Electrical conductivity* (pp. 377–414). New York: John Wiley.
- Fountain, A. (1994). Borehole water-level variations and implications for the subglacial hydraulics of South Cascade Glacier, Washington State, USA. *Journal of Glaciology*, 40(135), 293–304. <https://doi.org/10.3189/S002214300007383>
- Fox Maule, C., Parucker, M., & Olsen, N. (2009). Inferring magnetic crustal thickness and geothermal heat flux from crustal magnetic field models: Estimating the geothermal heat flux beneath the Greenland ice sheet (Tech. Rep.). Danish Meteorological Institute.
- Funk, M., Echelmeyer, K., & Iken, A. (1994). Mechanisms of fast flow in Jakobshavns Isbræ, West Greenland: Part II: Modeling of englacial temperatures. *Journal of Glaciology*, 40(136), 569–585. <https://doi.org/10.3189/172756502781831322>
- Glen, J. W. (1955). The creep of polycrystalline ice. *Proceedings of the Royal Society of London A: Mathematical, Physical and Engineering Sciences*, 228(1175), 519–538. <https://doi.org/10.1098/rspa.1955.0066>
- Gordon, S., Sharp, M., Hubbard, B., Smart, C., Ketterling, B., & Willis, I. (1998). Seasonal reorganization of subglacial drainage system of Haut Glacier d'Arolla, Valais, Switzerland, inferred from measurements in boreholes. *Hydrological Processes*, 12, 105–133.
- Gordon, S., Sharp, M., Hubbard, B., Willis, I., Smart, C., Copland, L., ... Ketterling, B. (2001). Borehole drainage and its implications for the investigation of glacier hydrology: experiences from Haut Glacier d'Arolla, Switzerland. *Hydrological Processes*, 15, 797–813. <https://doi.org/10.1002/hyp.184>
- Harper, J. T., Humphrey, N. F., Meierbachtol, T. W., Graly, J. A., & Fischer, U. H. (2017). Borehole measurements indicate hard bed conditions, Kangerlussuaq sector, western Greenland ice sheet. *Journal of Geophysical Research: Earth Surface*, 122, 1605–1618. <https://doi.org/10.1002/2017JF004201>
- Harrington, J. A., Humphrey, N. F., & Harper, J. T. (2015). Temperature distribution and thermal anomalies along a flowline of the Greenland ice sheet. *Journal of Glaciology*, 56(70), 98–104. <https://doi.org/10.3189/2015AoG70A945>
- Harrison, W. (1972). Temperature of a temperate glacier. *Journal of Glaciology*, 11(61), 15–29. <https://doi.org/10.3189/S0022143000022450>
- Hasholt, B., Mikkelsen, A., Nielsen, M., & Larsen, M. (2013). Observations of runoff and sediment and dissolved loads from the Greenland ice sheet at Kangerlussuaq, West Greenland, 2007 to 2010. *Zeitschrift für Geomorphologie*, 57(Suppl. 2), 3–27. <https://doi.org/10.1127/0372-8854/2012/S-00121>
- Hoffman, M. J., Andrews, L. C., Price, S. A., Catania, G. A., Neumann, T. A., Lüthi, M. P., ... Morriss, B. (2016). Greenland subglacial drainage evolution regulated by weakly connected regions of the bed. *Nature Communications*, 7, 13903.
- Hofstede, C., Christoffersen, P., Hubbard, B., Doyle, S. H., Young, T. J., Diez, A., ... Hubbard, A. (2018). Physical conditions of fast glacier flow: 2. Variable extent of anisotropic ice and soft basal sediment from seismic reflection data acquired on Store Glacier, West Greenland. *Journal of Geophysical Research: Earth Surface*, 123. <https://doi.org/10.1002/2017JF004297>
- Horgan, H. J., Anandakrishnan, S., Alley, R. B., Peters, L. E., Tsolias, G. P., Voigt, D. E., & Winberry, J. P. (2008). Complex fabric development revealed by englacial seismic reflectivity: Jakobshavn Isbræ, Greenland. *Geophysical Research Letters*, 35, L10501. <https://doi.org/10.1029/2008GL033712>
- How, P., Benn, D. I., Hulton, N. R. J., Hubbard, B., Luckman, A., Sevestre, H., ... Boot, W. (2017). Rapidly changing subglacial hydrological pathways at a tidewater glacier revealed through simultaneous observations of water pressure, supraglacial lakes, meltwater plumes and surface velocities. *The Cryosphere*, 11(6), 2691–2710. <https://doi.org/10.5194/tc-11-2691-2017>
- Howat, I., Box, J., Ahn, Y., Herrington, A., & McFadden, E. (2010). Seasonal variability in the dynamics of marine-terminating outlet glaciers in Greenland. *Journal of Glaciology*, 56(198), 601–613. <https://doi.org/10.3189/002214310793146232>
- Howat, I. M., & Eddy, A. (2011). Multi-decadal retreat of Greenland's marine-terminating glaciers. *Journal of Glaciology*, 57(203), 389–396. <https://doi.org/10.3189/002214311796905631>
- Howat, I. M., Negrete, A., & Smith, B. E. (2014). The Greenland Ice Mapping Project (GIMP) land classification and surface elevation datasets. *The Cryosphere Discussions*, 8(1), 453–478. <https://doi.org/10.5194/tcd-8-453-2014>
- Hubbard, B., & Nienow, P. (1997). Alpine subglacial hydrology. *Quaternary Science Reviews*, 16, 939–955. [https://doi.org/10.1016/S0277-3791\(97\)00031-0](https://doi.org/10.1016/S0277-3791(97)00031-0)
- Hubbard, B., Sharp, M., Willis, I., Nielsen, M., & Smart, C. (1995). Borehole water-level variations and the structure of the subglacial hydrological system of Haut Glacier d'Arolla, Valais, Switzerland. *Journal of Glaciology*, 41(139), 572–583. <https://doi.org/10.3189/S0022143000034894>
- Humphrey, N., & Echelmeyer, K. (1990). Hot-water drilling and borehole closure in cold ice. *Journal of Glaciology*, 36(124), 287–298. <https://doi.org/10.3189/002214390793701354>
- Humphrey, N., Kamb, B., Fahnestock, M., & Engelhardt, H. (1993). Characteristics of the bed of the lower Columbia Glacier, Alaska. *Journal of Geophysical Research*, 98(B1), 837–846. <https://doi.org/10.3189/002214390793701354>
- Iken, A., Echelmeyer, K., Harrison, W., & Funk, M. (1993). Mechanisms of fast flow in Jakobshavns Isbræ, West Greenland. I: Measurements of temperature and water level in deep boreholes. *Journal of Glaciology*, 39(131), 15–25. <https://doi.org/10.3189/S0022143000015689>
- Iken, A., Fabri, K., & Funk, M. (1996). Water storage and subglacial drainage conditions inferred from borehole measurements on Gornergletscher, Valais, Switzerland. *Journal of Glaciology*, 42(141), 233–248. <https://doi.org/10.3189/S0022143000004093>
- Iken, A., Rothlisberger, H., Flotron, A., & Haeberli, W. (1983). The uplift of Unteraargletscher at the beginning of the melt season—A consequence of water storage at the bed. *Journal of Glaciology*, 29(101), 28–47. <https://doi.org/10.3189/S0022143000005128>
- Iverson, N., Hanson, B., Hooke, R. L., & Jansson, P. (1995). Flow mechanism of glaciers on soft beds. *Science*, 267(5194), 80–81. <https://doi.org/10.1126/science.267.5194.80>
- Iverson, N. R., Hooyer, T. S., & Baker, R. W. (1998). Ring-shear studies of till deformation: Coulomb-plastic behavior and distributed strain in glacier beds. *Journal of Glaciology*, 44(148), 634–642. <https://doi.org/10.3189/S0022143000002136>
- Joughin, I., Das, S., King, M., Smith, B., Howat, I., & Moon, T. (2008). Seasonal speedup along the western flank of the Greenland Ice Sheet. *Science*, 320, 781–783. <https://doi.org/10.1126/science.1153288>
- Joughin, I., Howat, I. M., Fahnestock, M., Smith, B., Krabill, W., Alley, R. B., ... Truffer, M. (2008). Continued evolution of Jakobshavn Isbræ following its rapid speedup. *Journal of Geophysical Research*, 113, F04006. <https://doi.org/10.1029/2008JF001023>

- Joughin, I., Smith, B., Howat, I., & Scambos, T. (2011). MEaSUREs Greenland ice velocity: Selected glacier site velocity maps from InSAR. Wcoast-69.10n (Updated in 2014).
- Kalnay, E., Kanamitsu, M., Kistler, R., Collins, W., Deaven, D., Gandin, L., ... Joseph, D. (1996). The NCEP/NCAR 40-year reanalysis project. *Bulletin of the American Meteorological Society*, 77(3), 437–471.
- Kamb, B. (1987). Glacier surge mechanism based on linked-cavity configuration of the basal water conduit system. *Journal of Geophysical Research*, 92(B9), 9083–9100. <https://doi.org/10.1029/JB092iB09p09083>
- Kamb, B., & Engelhardt, H. (1987). Waves of accelerated motion in a glacier approaching surge: The mini-surges of Varigated Glacier, Alaska, U.S.A. *Journal of Glaciology*, 33(113), 27–46. <https://doi.org/10.3189/S0022143000005311>
- Kamb, B., Engelhardt, H., Fahnestock, M. A., Humphrey, N., Meier, M., & Stone, D. (1994). Mechanical and hydrologic basis for the rapid motion of a large tidewater glacier: 2. Interpretation. *Journal of Geophysical Research*, 99(B8), 15,231–15,244. <https://doi.org/10.1029/94JB00467>
- Kamb, B., Raymond, C., Harrison, W., Engelhardt, H., Echelmeyer, K., Humphrey, N., ... Pfeffer, T. (1985). Glacier surge mechanism: 1982–1983 surge of Varigated Glacier, Alaska. *Science*, 227(4686), 469–479. <https://doi.org/10.1126/science.227.4686.469>
- Karlssohn, N. B., Dahl-Jensen, D., Gogineni, S. P., & Paden, J. D. (2013). Tracing the depth of the Holocene ice in North Greenland from radio-echo sounding data. *Annals of Glaciology*, 54(64), 44–50. <https://doi.org/10.3189/2013AoG64A057>
- King, M. (2004). Rigorous GPS data-processing strategies for glaciological applications. *Journal of Glaciology*, 50(171), 601–607. <https://doi.org/10.3189/172756504781829747>
- Lüthi, M. (1999). Experimental and numerical investigation of a firn covered cold glacier and a polythermal ice stream: Case studies at Colle Gniffetti and Jakobshavn Isbræ (PhD thesis). Swiss Federal Institute of Technology Zurich.
- Lüthi, M., Funk, M., Iken, A., Gogineni, S., & Truffer, M. (2002). Mechanisms of fast flow in Jakobshavn Isbræ, West Greenland: Part III. Measurements of ice deformation, temperature and cross-borehole conductivity in boreholes to the bedrock. *Journal of Glaciology*, 48(162), 369–385. <https://doi.org/10.3189/172756502781831322>
- Lüthi, M., Fahnestock, M., & Truffer, M. (2009). Calving icebergs indicate a thick layer of temperate ice at the base of Jakobshavn Isbræ, Greenland. *Journal of Glaciology*, 55(191), 563–566. <https://doi.org/10.3189/002214309788816650>
- Lüthi, M. P., Funk, M., & Iken, A. (2003). Indication of active overthrust faulting along the Holocene-Wisconsin transition in the marginal zone of Jakobshavn Isbræ. *Journal of Geophysical Research*, 108(B11), 2543. <https://doi.org/10.1029/2003JB002505>
- Lüthi, M. P., Ryser, C., Andrews, L. C., Catania, G. A., Funk, M., Hawley, R. L., ... Neumann, T. A. (2015). Heat sources within the Greenland Ice Sheet: Dissipation, temperate paleo-firn and cryo-hydrologic warming. *The Cryosphere*, 9(1), 245–253. <https://doi.org/10.5194/tc-9-245-2015>
- Makinson, K., & Anker, P. (2014). The BAS ice-shelf hot-water drill: Design, methods and tools. *Annals of Glaciology*, 55(68), 44–52. <https://doi.org/10.3189/2014AoG68A030>
- Mankoff, K. D., & Tulaczyk, S. M. (2017). The past, present, and future viscous heat dissipation available for Greenland subglacial conduit formation. *The Cryosphere*, 11(1), 303–317. <https://doi.org/10.5194/tc-11-303-2017>
- Meier, M., Lundsrom, S., Stone, D., Kamb, B., Engelhardt, H., Humphrey, N., ... Walters, R. (1994). Mechanical and hydrologic basis for the rapid motion of a large tidewater glacier 1. Observations. *Journal of Geophysical Research*, 99(B8), 15,219–15,229. <https://doi.org/10.1029/94JB00237>
- Meierbachtol, T., Harper, J., & Humphrey, N. (2013). Basal drainage system response to increasing surface melt on the Greenland ice sheet. *Science*, 341(6147), 777–779. <https://doi.org/10.1126/science.1235905>
- Meierbachtol, T., Harper, J., Humphrey, N., & Wright, P. (2016). Mechanical forcing of water pressure in a hydraulically isolated reach beneath Western Greenland's ablation zone. *Annals of Glaciology*, 52(72), 62–70. <https://doi.org/10.1017/aog.2016.5>
- Moon, T., Joughin, I., Smith, B., van den Broeke, M. R., van de Berg, W. J., Noël, B., & Usher, M. (2014). Distinct patterns of seasonal Greenland glacier velocity. *Geophysical Research Letters*, 41, 7209–7216. <https://doi.org/10.1002/2014GL061836>
- Motyka, R. J., Truffer, M., Fahnestock, M., Mortensen, J., Rysgaard, S., & Howat, I. (2011). Submarine melting of the 1985 Jakobshavn Isbræ floating tongue and the triggering of the current retreat. *Journal of Geophysical Research*, 116, F01007. <https://doi.org/10.1029/2009JF001632>
- Murray, T. (1997). Assessing the paradigm shift: Deformable glacier beds. *Quaternary Science Reviews*, 16(9), 995–1016. [https://doi.org/10.1016/S0277-3791\(97\)00030-9](https://doi.org/10.1016/S0277-3791(97)00030-9)
- Murray, T., & Clarke, G. (1995). Black-box modelling of the subglacial water system. *Journal of Geophysical Research*, 100, 10,231–10,245. <https://doi.org/10.1029/95JB00671>
- Nettles, M., Larsen, T., Elósegui, P., Hamilton, G., Stearns, L., Ahlström, A., ... Forsberg, R. (2008). Step-wise changes in glacier flow speed coincide with calving and glacial earthquakes at Helheim Glacier, Greenland. *Geophysical Research Letters*, 35, L24503. <https://doi.org/10.1029/2008GL036127>
- Nick, F. M., Vieli, A., Andersen, M. L., Joughin, I., Payne, A., Edwards, T. L., ... van de Wal, R. S. W. (2013). Future sea-level rise from Greenland's main outlet glaciers in a warming climate. *Nature*, 497(7448), 235–238. <https://doi.org/10.1038/nature12068>
- Nye, J. F. (1957). The distribution of stress and velocity in glaciers and ice-sheets. *Proceedings of the Royal Society of London A: Mathematical, Physical and Engineering Sciences*, 239(1216), 113–133. <https://doi.org/10.1098/rspa.1957.0026>
- Orwin, J. F., & Smart, C. C. (2004). Short-term spatial and temporal patterns of suspended sediment transfer in proglacial channels, Small River Glacier, Canada. *Hydrological Processes*, 18(9), 1521–1542. <https://doi.org/10.1002/hyp.1402>
- Orwin, J. F., & Smart, C. C. (2005). An inexpensive turbidimeter for monitoring suspended sediment. *Geomorphology*, 68(1), 3–15. <https://doi.org/10.1016/j.geomorph.2004.04.007>
- Paterson, W. (1991). Why ice-age ice is sometimes “soft”. *Cold Regions Science and Technology*, 20(1), 75–98. [https://doi.org/10.1016/0165-232X\(91\)90058-O](https://doi.org/10.1016/0165-232X(91)90058-O)
- Perol, T., & Rice, J. R. (2015). Shear heating and weakening of the margins of West Antarctic ice streams. *Geophysical Research Letters*, 42, 3406–3413. <https://doi.org/10.1002/2015GL063638>
- Pollack, H. N., Hurter, S. J., & Johnson, J. R. (1993). Heat flow from the Earth's interior: Analysis of the global data set. *Reviews of Geophysics*, 31(3), 267–280. <https://doi.org/10.1029/93RG01249>
- Rignot, E., Box, J. E., Burgess, E., & Hanna, E. (2008). Mass balance of the Greenland ice sheet from 1958 to 2007. *Geophysical Research Letters*, 35, L20502. <https://doi.org/10.1029/2008GL035417>
- Rignot, E., Koppes, M., & Velicogna, I. (2010). Rapid submarine melting of the calving faces of West Greenland glaciers. *Nature Geoscience*, 3, 187–191. <https://doi.org/10.1038/NGEO765>
- Rogozhina, I., Hagedoorn, J. M., Martinez, Z., Fleming, K., Soucek, O., Greve, R., & Thomas, M. (2012). Effects of uncertainties in the geothermal heat flux distribution on the Greenland ice sheet: An assessment of existing heat flow models. *Journal of Geophysical Research*, 117, F02025. <https://doi.org/10.1029/2011JF002098>

- Rogozhina, I., Petrunin, A. G., Vaughan, A. P. M., Steinberger, B., Johnson, J. V., Kaban, M. K., ... Koulakov, I. (2016). Melting at the base of the Greenland ice sheet explained by Iceland hotspot history. *Nature Geoscience*, 9(5), 366–369. <https://doi.org/10.1038/ngeo2689>
- Röthlisberger, H. (1972). Water pressure in intra- and subglacial channels. *Journal of Glaciology*, 11(62), 177–203. <https://doi.org/10.3189/S002214300022188>
- Ryan, J. C., Hubbard, A. L., Todd, J., Carr, J. R., Box, J. E., Christoffersen, P., ... Snooke, N. (2014). Repeat UAV photogrammetry to assess calving front dynamics at a large outlet glacier draining the Greenland ice sheet. *The Cryosphere Discussions*, 8(2), 2243–2275. <https://doi.org/10.5194/tcd-8-2243-2014>
- Ryser, C. (2014). Cold ice in an alpine glacier and ice dynamics at the margin of the Greenland ice sheet (PhD thesis). ETH Zürich.
- Ryser, C., Lüthi, M. P., Andrews, L. C., Hoffman, M. J., Catania, G. A., Hawley, R. L., ... Kristensen, S. S. (2014). Sustained high basal motion of the Greenland ice sheet revealed by borehole deformation. *Journal of Glaciology*, 60(222), 647–660. <https://doi.org/10.3189/2014JoG13J196>
- Ryser, C., Lüthi, M., Andrews, L., Catania, G., Funk, M., Hawley, R., ... Neumann, T. (2014). Caterpillar-like ice motion in the ablation zone of the Greenland ice sheet. *Journal of Geophysical Research: Earth Surface*, 119, 2258–2271. <https://doi.org/10.1002/2013JF003067>
- Schaer, S., Gurtner, W., & Feltns, J. (1998). IONEX: The IONosphere map EXchange Format Version 1. In *Proceedings of the IGS AC Workshop*. Darmstadt, Germany.
- Shapiro, D. R., Joughin, I. R., Poinar, K., Morlighem, M., & Gillet-Chaulet, F. (2016). Basal resistance for three of the largest Greenland outlet glaciers. *Journal of Geophysical Research: Earth Surface*, 121, 168–180. <https://doi.org/10.1002/2015JF003643>
- Shapiro, N. M., & Ritzwoller, M. H. (2004). Inferring surface heat flux distributions guided by a global seismic model: particular application to Antarctica. *Earth and Planetary Science Letters*, 223(1-2), 213–224. <https://doi.org/10.1016/j.epsl.2004.04.011>
- Smart, C. C. (1996). Statistical evaluation of glacier boreholes as indicators of basal drainage systems. *Hydrological Processes*, 10(4), 599–613. [https://doi.org/10.1002/\(SICI\)1099-1085\(199604\)10:4<599::AID-HYP394>3.0.CO;2-8](https://doi.org/10.1002/(SICI)1099-1085(199604)10:4<599::AID-HYP394>3.0.CO;2-8)
- Smeets, C., Boot, W., Hubbard, A., Pettersson, R., Wilhelms, F., Van Den Broeke, M., & Van De Wal, R. (2012). Instruments and methods—A wireless subglacial probe for deep ice applications. *Journal of Glaciology*, 58(211), 841–848. <https://doi.org/10.3189/2012JoG11J130>
- Steinhart, J., & Hart, S. (1968). Calibration curves for thermistors. *Deep Sea Research and Oceanographic Abstracts*, 15(4), 497–503. [https://doi.org/10.1016/0011-7471\(68\)90057-0](https://doi.org/10.1016/0011-7471(68)90057-0)
- Stone, D., & Clarke, G. (1993). Estimation of subglacial hydraulic properties from induced changes in basal water pressure: A theoretical framework for borehole-response tests. *Journal of Glaciology*, 39(132), 327–340. <https://doi.org/10.3189/S0022143000015999>
- Stone, D., Clarke, G., & Blake, E. (1993). Subglacial measurement of turbidity and electrical conductivity. *Journal of Glaciology*, 39(13), 415–420. <https://doi.org/10.3189/S0022143000016075>
- Stone, D. B., & Clarke, G. K. C. (1996). In situ measurements of basal water quality and pressure as an indicator of the character of subglacial drainage systems. *Hydrological Processes*, 10(4), 615–628. [https://doi.org/10.1002/\(SICI\)1099-1085\(199604\)10:4<615::AID-HYP395>3.0.CO;2-M](https://doi.org/10.1002/(SICI)1099-1085(199604)10:4<615::AID-HYP395>3.0.CO;2-M)
- Straneo, F., Hamilton, G., Sutherland, D., Stearns, L., Davidson, F., Stenson, G., & Rosing-Asvid, A. (2010). Rapid circulation of warm subtropical waters in a major glacial fjord in East Greenland. *Nature Geoscience*, 3(3), 182–186. <https://doi.org/10.1038/ngeo764>
- Suckale, J., Platt, J. D., Perol, T., & Rice, J. R. (2014). Deformation-induced melting in the margins of the West Antarctic ice streams. *Journal of Geophysical Research: Earth Surface*, 119, 1004–1025. <https://doi.org/10.1002/2013JF003008>
- Sugiyama, S., & Gudmundsson, G. H. (2003). Diurnal variations in vertical strain observed in a temperate valley glacier. *Geophysical Research Letters*, 30(2), 1090. <https://doi.org/10.1029/2002GL016160>
- Sugiyama, S., Skvarca, P., Naito, N., Enomoto, H., Tsutaki, S., Tone, K., ... Aniya, M. (2011). Ice speed of a calving glacier modulated by small fluctuations in basal water pressure. *Nature Geoscience*, 4(9), 597–600. <https://doi.org/10.1038/ngeo116075>
- Thomsen, H., Olesen, O., Braithwaite, R., & Boggild, C. (1991). Ice drilling and mass balance at Pakitsoq, Jakobshavn, central West Greenland, Report 152. Copenhagen, Denmark: Grønlands Geologiske Undersøgelse.
- Todd, J., & Christoffersen, P. (2014). Are seasonal calving dynamics forced by buttressing from ice mélange or undercutting by melting? Outcomes from full-stokes simulations of Store Glacier, West Greenland. *The Cryosphere*, 8(6), 2353–2365. <https://doi.org/10.5194/tc-8-2353-2014>
- van As, D. (2011). Warming, glacier melt and surface energy budget from weather station observations in the Melville Bay region of northwest Greenland. *Journal of Glaciology*, 57(202), 208–220. <https://doi.org/10.3189/002214311796405898>
- van de Wal, R. S. W., Smeets, C. J. P. P., Boot, W., Stoffelen, M., van Kampen, R., Doyle, S. H., ... Hubbard, A. (2015). Self-regulation of ice flow varies across the ablation area in south-west Greenland. *The Cryosphere*, 9(2), 603–611. <https://doi.org/10.5194/tc-9-603-2015>
- Van Tricht, K., Lhermitte, S., Lenaerts, J. T. M., Gorodetskaya, I. V., L'Ecuyer, T. S., Noel, B., ... van Lipzig, N. P. M. (2016). Clouds enhance Greenland ice sheet meltwater runoff. *Nature Communications*, 7, 10266. <https://doi.org/10.1038/ncomms10266>
- Vieli, A., Jania, J., Blatter, H., & Funk, M. (2004). Short-term velocity variations on Hansbreen, a tidewater glacier in Spitsbergen. *Journal of Glaciology*, 50(170), 389–398. <https://doi.org/10.3189/172756504781829963>
- Waddington, B. S., & Clarke, G. K. (1995). Hydraulic properties of subglacial sediment determined from the mechanical response of water-filled boreholes. *Journal of Glaciology*, 41(137), 112–124. <https://doi.org/10.3189/S0022143000017810>
- Walder, J., & Fowler, A. (1994). Channelized subglacial drainage over a deformable bed. *Journal of Glaciology*, 40(134), 3–15. <https://doi.org/10.3189/S0022143000003750>
- Walter, F., Chaput, J., & Luthi, M. (2014). Thick sediments beneath Greenland's ablation zone and their potential role in future ice sheet dynamics. *Geology*, 42(6), 487–490. <https://doi.org/10.1130/G35492.1>
- Walter, J. I., Box, J. E., Tulaczyk, S., Brodsky, E. E., Howat, I. M., Ahn, Y., & Brown, A. (2012). Oceanic mechanical forcing of a marine-terminating Greenland glacier. *Annals of Glaciology*, 53(60), 181–192. <https://doi.org/10.3189/2012AoG60A083>
- Weidick, A. (1995). *Satellite image atlas of glaciers of the world*, chap. Greenland. (pp. C1–C105). Denver, CO: USGS Professional Paper 1386-C, US Geological Survey.
- Wright, P. J., Harper, J. T., Humphrey, N. F., & Meierbachtol, T. W. (2016). Measured basal water pressure variability of the western Greenland ice sheet: Implications for hydraulic potential. *Journal of Geophysical Research: Earth Surface*, 121, 1134–1147. <https://doi.org/10.1002/2016JF003819>
- Xu, Y., Rignot, E., Fenty, I., Menemenlis, D., & Flexas, M. M. (2013). Subaqueous melting of Store Glacier, west Greenland from three-dimensional, high-resolution numerical modeling and ocean observations. *Geophysical Research Letters*, 40, 4648–4653. <https://doi.org/10.1002/grl.50825>
- Young, T., Christoffersen, P., Nicholls, K., Lok, L., Doyle, S., Hubbard, B., ... Hubbard, A. (2016). High basal melt rates observed on Store Glacier, West Greenland, using phase-sensitive FMCW radar. In *AGU Fall Meeting Abstracts C33A-0769*.